UC San Diego

UC San Diego Electronic Theses and Dissertations

Title

Patient-specific modeling of cardiac geometry in dyssynchronous heart failure

Permalink

https://escholarship.org/uc/item/3q4225tf

Author

Sheth, Mansi N.

Publication Date

2010

Peer reviewed|Thesis/dissertation

eScholarship.org Powered by the California Digital Library
University of California

UNIVERSITY OF CALIFORNIA, SAN DIEGO

PATIENT-SPECIFIC MODELING OF CARDIAC GEOMETRY IN DYSSYNCHRONOUS HEART FAILURE

A thesis submitted in partial satisfaction of the requirements
for the degree Master of Science

in

Bioengineering

by

Mansi N. Sheth

Committee in charge:

Professor Andrew McCulloch, Chair
Professor David Krummen
Professor Jeffery Omens

2010

Copyright
Mansi N. Sheth, 2010
All rights reserved.

The thesis of Mansi N. Sheth is approved, and it is acceptable in quality and form for publication on microfilm and electronically:

_____

_____

_____

Chair

University of California, San Diego

2010

TABLE OF CONTENTS

Signature Page iii
Table of Contents iv
List of Figures vi
List of Tables viii
Acknowledgements ix
Abstract of the Thesis x
1 Background 1
1.1 Cardiac Anatomy 1
1.1 Cardiac Function 3
1.2 Congestive Heart Failure 6
1.3 Cardiac resynchronization Therapy 8
1.4 Computational Modeling 9
1.5 Finite Element Modeling of Cardiac Anatomy 11
1.6 Image-based Cardiac Models 13
1.7 Ventricular Geometry 15
1.8 Goals 17
2 Materials and Methods 20
2.1 Patient Selection and Bi-Ventricular Implantation 20
2.2 Clinical Measurements 21
2.2.1 Computed Tomography and Magnetic Resonance Imaging 21
2.3 Data Processing and Model Development 22
2.3.1 Image Segmentation 23
2.3.2 Landmark Points 25
2.3.3 Image Transformation 26
2.3.4 Rectangular Cartesian to Prolate Spheroidal Coordinates 29
2.3.5 Initial Finite Element Mesh Set up 31
2.3.6 Two-dimensional Mesh Fitting 35
2.3.7 Three-dimensional Mesh Generation 37

2.4 Myocardial Thickness Estimation 37
2.5 Ventricular Cavity and Myocardial Volume Estimation 38
3 Results 39
3.1 Image Segmentation 39
3.1 Landmark Points 41
3.2 Image transformation and Model Development 42
3.3 Myocardial Wall Thickness Estimation 50
3.4 Ventricular Cavity and Wall Volume Estimation 52
4 Discussion 54
4.1 Image Segmentation 55
4.2 Model Development 56
4.3 Myocardial Wall Thickness Estimation 59
4.4 Ventricular Cavity and Wall Volume Estimation 60
5 Conclusion 62
6 Appendices 65
6.1 Appendix A 65
6.2 Appendix B 69
6.3 Appendix C 71
References 79

LIST OF FIGURES

Figure 1-1: Longitudinal cross-section of the heart. 2
Figure 1-2: Schematic diagram of left ventricular pressure–volume loops. 5
Figure 1-3: Figure showing the general curvilinear coordinates ((ξ_1, ξ_2, ξ_3).. 12
Figure 1-4: Ventricular geometry represented as a truncated ellipsoid. 16
Figure 1-5: Workflow for design of patient-specific model to predict response to CRT.. 19
Figure 2-1:Process of Image Segmentation 25
Figure 2-2: Posterior view of the initial mesh developed from the 17 landmark points 33
Figure 2-3: Posterior and anterior view of the initial mesh with data points..... 33
Figure 2-4: Posterior top view of the initial mesh developed for patient 2 showing the data points derived from segmentation. 34
Figure 2-5: Posterior view of the initial mesh with data points for patient 2. 34
Figure 2-6: Posterior top view of the initial mesh for patient 2 showing data points from segmentation. 35
Figure 3-1: Stack of images obtained from CT 40
Figure 3-2: Stack of images showing the segmented endocardium and epicardium 40
Figure 3-3: Data points showing the posterior and top view of the human heart. 41
Figure 3-4: CT slice showing segmented contours and four of seventeen landmark points. 41
Figure 3-5: Spatial distribution of all the seventeen landmark points 42
Figure 3-6: Data points aligned according to the CT coordinate system for patient 1. .. 43
Figure 3-7: Data points translated to adjust the origin at two-thirds from apex to base and rotated to align the x-axis along the long axis of the heart and the y-axis bisecting the septum and RVFW**.** 43
Figure 3-8: Posterior view of the fitted mesh and top posterior view of the fitted mesh with data points for patient 1. 45
Figure 3-9: Fitted endocardium and fitted epicardium with data points for patient 1. ... 45
Figure 3-10: Biventricular patient-specific model of the failing heart of patient 1. 46

Figure 3-11: Three-dimensional model of the human heart (patient 1) showing the $x_i(1)$ and $x_i(2)$ coordinates. 46
Figure 3-12: Top posterior view of the three-dimensional patient-specific model of human heart (patient 1). 47
Figure 3-13: Fitted patient-specific model showing endocardial surfaces of the failing heart of patient 2. 48
Figure 3-14: Fitted patient-specific model showing epicardial surface of failing heart of patient 2. 48
Figure 3-15: Posterior top view of the fitted model showing data points obtained from segmentation of MR images of patient 2. 49
Figure 3-16: 3D model showing $x_i(1)$ and $x_i(2)$ surfaces of the failing heart of patient 2. 49
Figure 3-17: Diagram showing 17 segment circumferential polar plot and the recommended nomenclature for tomographic imaging of the heart 51
Figure 3-18: Bull's eye plot showing the spatial distribution of myocardial wall thickness in patient 2. 51
Figure 3-19: Bull's eye plot showing the spatial distribution of myocardial wall thickness in patient 2. 52
Figure 4-1: Posterior view of the initial mesh built using connected nodes and after rotating nodes in Matlab. 58

LIST OF TABLES

Table 1-1: Table showing NYHA classification of heart failure patients 7
Table 3-1- Table comparing the SWT and PWT calculated using 3D Model and Echocardiograms..... 50
Table 3-2- Table showing the cavity and wall volume and mass 52
Table 3-3: Table comparing the LV cavity volume calculated using 3D model and Simpson's rule 53

ACKNOWLEDGEMENTS

I would like to express my heartfelt gratitude to my Professors, family and friends for their support and guidance in helping me reach this stage of my life. I would like to first and foremost thank my advisor, Dr. Andrew McCulloch for his guidance, advice and patience throughout my time with the Cardiac Mechanics Research Group at UCSD. This work would not have been possible without his insights, expertise and invaluable input towards reaching the goal of this research.

I would also like to thank other members of the lab for training me and always willing to help me when I needed it the most. In particular, I would like to thank Dr. Roy Kerckhoffs for his very helpful suggestions and patience in training me to get started with my research and with editing my thesis, Dr. David Krummen for his help with data acquisition for the research, guidance on reading CT and MRI data and input on my thesis, Dr. Jeffery Omens for help with editing my thesis, Jeff Van Dorn for lending his expertise in the field of python programming for Continuity, Fred Lionetti for helping me learn and get accustomed to Continuity in a very short period of time, and Chris Villongco and Joyce Chuang for always offering to help and guide me.

Lastly, I would like to express my love and thankfulness to my parents and sister for always standing by me, for loving, supporting and always believing in me. I would also like to thank Varun Krovi for his support all throughout. I am very grateful for all their motivation and encouragement towards achieving my goals.

ABSTRACT OF THE THESIS

PATIENT-SPECIFIC MODELING OF CARDIAC GEOMETRY IN DYSSYNCHRONOUS HEART FAILURE

by

Mansi N. Sheth

Master of Science in Bioengineering
University of California, San Diego, 2010

Professor Andrew McCulloch, Chair

Cardiac resynchronization therapy (CRT) is the currently used non-pharmacologic therapy for heart failure (HF) patients with a conduction disturbance. The purpose of CRT is to resynchronize contraction between and within ventricles. This dyssynchrony arises from an abnormality in the heart's electrical conducting system that causes the two ventricles to beat asynchronously. Studies from clinical trials have shown that about 30% of the patients do not gain any benefits from CRT. Computational models may have the potential to predict the response of patients to CRT and could be used to optimize the effects of this therapy. Hence, we have developed

methods for generating anatomically detailed patient-specific three-dimensional finite element models of the failing human heart from clinical measurements. Two three-dimensional finite element models were generated from cardiac computed tomography and magnetic resonance images obtained at end-diastole using a newly developed semi-automatic technique of landmark points. Landmark points are anatomical locations identified on the cardiac images that allow us to estimate the extent of the heart in order to build a 3D model of the failing heart. Seventeen landmark points were used to precisely determine the circumferential and longitudinal extent of the failing human heart. A 3D finite element model with 50 nodes and 24 elements was generated for two patients with dyssynchronous heart failure. These 3D models were then used to estimate myocardial wall thickness and ventricular cavity volume. The method of landmark points provides an efficient way to generate finite-element meshes.

1 Background

1.1 Cardiac Anatomy

The heart is a muscular pump that pumps blood throughout the circulation while delivering nutrients and removing waste from each of the organs, and transporting vital hormones and other messengers to all parts of the body. Human heart is made up of four pumping chambers: the *right* and *left atria* (LA) and *right* and *left ventricles*(LV). There are two atrioventricular valves in the heart. The *tricuspid valve* is located on the right while the *mitral valve* is located on the left between the cavities of atria and ventricles. Oxygenated blood travels from the lungs through large vessels called pulmonary veins and enter the left side of the heart, emptying the blood into the left atrium. The pulmonary vein is the only vein in the body that carries oxygenated blood. All other veins carry deoxygenated blood from other parts of the body back to the heart. The blood from the left atrium now flows into the left ventricle through the mitral valve. About 70% of this inflow occurs when the heart is in the relaxed state. Upon contraction

of the atrium, the remaining 30% of the ventricle gets filled with blood. The ventricle contracts after a slight delay. At this point the atrioventricular valve closes and prevents the back flow of blood into the atrium. Due to the contraction, the blood is forced to exit via the left ventricular outflow tract that leads to the aorta. A detailed illustration of the heart is shown in Figure 1-1.

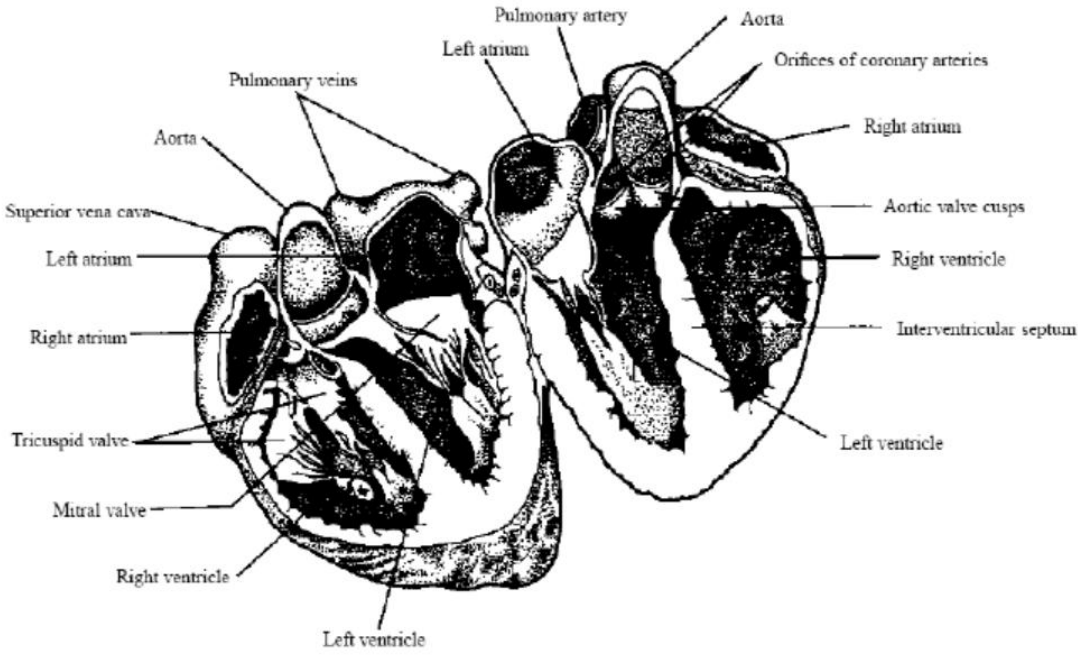

Figure 1-1: Longitudinal cross-section of the heart. Source: Katz 2001 [1].

Another type of valve called *semilunar* separates the outflow tracts of both ventricles and their respective outflow artery. Blood flows from the right ventricle (RV) to the pulmonary artery through the *pulmonic* valve and blood flows from the left ventricle to the aorta through the *aortic* valve. Various arteries branch out of the aorta carrying oxygenated blood to all parts of the body. The deoxygenated blood flows into the body tissues eventually though capillaries. Before entering the right side of the

heart, the blood flows through a series of veins. The superior vena cava drains the upper body, and the inferior vena cava drains the lower body. Both the type of valves, atrioventricular and semilunar, are distinct from each other. While the atrioventricular valves have their large cusps supported at their free ends by *chordae tendinae* (fibrous cords) that attach to *papillary muscles* that arise from the inner walls of the right and left ventricular cavities, the semilunar valve cusps are supported at their margins by thick, tendinous fibers.

1.1 Cardiac Function

The primary function of the heart is to pump blood throughout the body. The regular and continuous contraction of the heart muscle, generates and sustains an arterial blood pressure required to provide adequate perfusion of organs. Each cardiac contraction undergoes a series of electrical and mechanical events that lead to the opening and closing of the valves, flow of blood into and out of the heart, and the timing of the heart sounds forming a cardiac cycle. The frequency of a cardiac cycle is the heart rate. A cardiac cycle can be divided into two phases; systole and diastole. The walls of the ventricle go through a sequence of changes in pressure and length during each cardiac cycle which can be displayed as a work diagram called a “pressure-volume loop” where pressure is plotted as a function of volume. The pressure-volume loop begins at end-diastole and passes through four phases. *Isovolumic contraction* is the first phase of systole which begins when tension is developed by the ventricular myocardium. An increase in the intraventricular pressure first closes the mitral valve. The ventricular pressure continues to rise until it exceeds that in the aorta and thus,

aortic valve opens (AVO). The second phase, *ejection* wherein aortic pressure (afterload) first rises because the blood is flowing into the aorta faster than it is running out into the tissues and then falls as the slowing of ejection allows blood to run out of the aorta more rapidly than it enters from the ventricle. Systole ends at a point along the *end-systolic pressure-volume relationship* (ESPVR). The third phase, *isovolumic relaxation* is when both the aortic and mitral valves are closed. Diastole begins with isovolumic relaxation. Diastole continues when the left ventricular pressure falls below the left atrium and the mitral valve opens (MVO) and thus, initiating the final phase *filling* (preload). Blood now flows across the mitral valve from the atrium into the relaxed ventricle. Left ventricular pressure and volume gradually rises during this phase. Diastole ends at a point on the *end-diastole pressure-volume relationship* (EDPVR). Filling is influenced by the geometry and thickness of the left ventricular walls and the material properties of the myocardium. Figure 1-2 shows a schematic representation of the left ventricular pressure-volume loops.

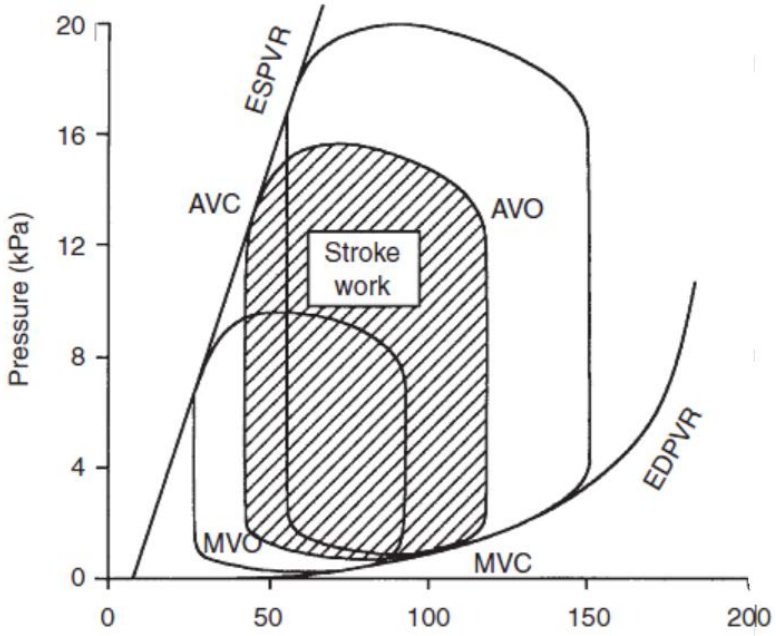

Figure 1-2: Schematic diagram of left ventricular pressure–volume loops. End-systolic pressure–volume relation (ESPVR), end-diastolic pressure–volume relation (EDPVR) and stroke work are shown. The effects of changes in preload and afterload are shown by the three P-V loops. Source: McCulloch AD 2005 [3].

Changes in cardiac function associated with HF results in a decrease in cardiac output (CO). Cardiac output is the volume of blood being pumped by the heart per minute. CO is a function of heart rate (HR) and stroke volume (SV).

$$CO = HR \times SV$$

The stroke volume is given by the difference between the end-diastolic volume (EDV) and the end-systolic volume (ESV).

In this project, emphasis was placed on the geometrical properties of the failing heart including wall thickness and end-diastolic volume of the wall, LV and RVFW cavity volume from the 3D patient specific models. The importance of wall thickness in evaluating the mechanical performance of the left ventricle was recognized by Woods in 1892 in his attempt to apply the law of Laplace to the calculation of cardiac wall

tension, and Burton later emphasized the relation between the shape and size of the ventricle and the performance of the heart as a pump [22, 23]. In addition, the ratio between the cavity volume and wall volume provides useful insight into the amount of dilation of the heart.

1.2 Congestive Heart Failure

The epidemic of heart failure (HF) is a crucial public health issue that is faced by the health care system. The scope of the epidemic is profound. About 5 million Americans are diagnosed with heart failure, 600,000 incident cases, and 1 million hospitalizations occur annually at a cost of more than $25 billion [8]. The prevalence of HF increases considerably with age. According to Rotterdam study, <1% of individuals aged from 55 to 64 years are diagnosed with HF [9]. This increases to >17% in the ≥85-year age group. Even though the mortality rates for cardiovascular diseases have declined, hospitalization for heart failure has increased substantially. Hospital discharges for congestive heart failure in the Unites States has risen from 377,000 in 1979 to 999,000 in 2000, a 165% increase [10]. Recent estimates of total annual health-care expenses for HF in Americans have ranged from $10.3 to $37.8 billion [11,12]. An estimate of cumulative care costs during hospitalization ranges from $6000 to $12,000 per admission.

HF is a condition wherein the heart is unable to supply sufficient blood flow to meet the body's needs. Over time, conditions like narrowed arteries or high blood pressure leave the heart too weak or stiff to fill and pump efficiently. Typically, HF is caused due to myocardial infarction (heart attacks) and other forms of ischemic heart

disease, hypertension, valvular heart disease and cardiomyopathy. According to the New York Heart Association (NYHA) functional classification, patients can be categorized as being under 4 categories as described by Table 1-1 [13,14]:

Table 1-1: Table showing NYHA classification of heart failure patients

NYHA Class	Symptoms
I	No symptom or limitation in ordinary physical activity such as shortness of breath while walking etc.
II	Mild symptoms and slight limitation during ordinary activity.
III	Increased limitation in activity owing to symptoms even during less than ordinary activity.
IV	Severe limitation even at rest

HF treatments currently available can improve symptoms and help a weakened heart work as efficiently as possible. Several types of drugs are used in the treatment of HF like angiotensin-conerting enzyme (ACE) inhibitors, angiotensin II (A-II) receptor blockers, beta blockers and diuretics. Some patients also undergo surgery or use implantable medical devices to treat CHF. Patients with HF are also at a high risk of ventricular tachyarrhythmia, and may require Implantable Cardiac Defibrillators (ICD). Approximately a third of the CHF patients undergoing ICD implantation have abnormalities in their heart's electrical system which causes their heart to beat in an uncoordinated fashion [55]. Such patients are usually candidates for a Biventricular ICD.

Despite these current treatment options, the symptoms of CHF in patients often continue to worsen and admission rates in hospital remain high. [15]. HF still continues

to be a fatal disease with a survival rate of only 35% five years after patients have been first diagnosed [16]. CHF has been the area of intense research for years and huge collaborative efforts are being made by physicians and scientists to improve the understanding of this condition. A sincere effort is being made to improve the quality of life of patients diagnosed with CHF.

1.3 Cardiac resynchronization Therapy

Cardiac Resynchronization therapy (CRT) is a recently developed technique to treat dilated HF with dyssynchronous contraction. Typically, dyssynchrony due to LBBB in the heart arises from electrical delay that translates into mechanical delay between the septal and lateral walls. Primarily, CRT is given to HF patients with electrical timing delay. CRT or biventricular pacing is a novel therapy for patients with advanced HF and a conduction delay. In about 25% of patients with QRS>120ms, LV dyssynchrony occurs and is associated with a high mortality rate. It increases the risk of worsened failure and sudden cardiac death 1.7 fold [17].

A CRT device sends electrical impulses to both the lower chambers of the heart to facilitate the synchronous beating of the two chambers. This improves the ability of the heart to pump blood and oxygen to the body. The device consists of a pulse generator, a battery and insulated wires called leads. Leads are used to carry information signals from the heart to the device, and to carry electrical impulses to the heart. One lead delivers impulses to the RA and the other may deliver impulses to the RV. There is an additional lead that is positioned in a vein on the surface of the LV. With these leads in place, the CRT device can stimulate both the left and right ventricles

at the same time. There are two types of implantable CRT devices- CRT pacemaker and CRT pacemaker with defibrillator therapy that is used to treat fast heart rhythms.

Studies have demonstrated the safety and efficacy of CRT in patients with NYHA class III and IV HF. The efficacy of CRT is based on the reduction in the conduction delay between the two ventricles and optimization of the ejection fraction, lowering mitral regurgitation, LV remodeling leading to improved symptoms. CRT significantly improves LV structure and function, NYHA functional class, exercise tolerance, quality of life, and reduces morbidity and mortality. An important aspect of CRT is the selection of HF patients that will benefit from CRT. Clinical trials have shown that patients with NYHA class III-IV, mean left ventricular ejection fraction (LVEF) about 21% to 23% and a wide QRS (>120ms, mean 156-178ms) mainly resulting from LBBB and ischemic etiology benefit the most from CRT. There are up to 30% of the patients that are classified as non-responders. Current patient selection criteria for CRT, such as QRS duration of more than 120 ms, improvements in the distance walked in 6 minutes, peak oxygen utilization (VO2 max) during exercise, and a decrease in left ventricular end-systolic volume are not sufficient to distinguish responders from non-responders. This calls for newer ways to identify the patients who will benefit from CRT and develop alternate approach to treating HF.

1.4 Computational Modeling

Computational Models are becoming increasingly popular with advances in computer power, novel diagnostic and therapeutic medical technologies, and an increasing knowledge of pathophysiology from gene to organ systems. These have

allowed for the application of multiscale patient-specific modeling based on proven disease mechanism. The importance of these models lies in the fact that they can be effectively used in the guidance and prediction of response to therapy in different areas of medicine. Patient-specific models have been developed in many areas of human physiology. These models are useful in clinical settings to predict and optimize the outcome from surgery and non-invasive therapy. Cardiac computational models can be used to make the response to CRT more effective. *Continuity 6.3*, a problem-solving environment for multiscale modeling and data analysis in bioengineering and physiology, is an efficient tool for finite element modeling in cardiac biomechanics, biotransport and electrophysiology. It is distributed free for academic research by the National Biomedical Computation Resource and can be downloaded at http://www.continuity.ucsd.edu/Continuity. Finite element method (FEM) is a numerical technique most commonly used in computational modeling of the heart. The complex 3D geometry of the heart is discretized into multiple elements and nodes. FEM solves partial differential equations that govern the mechanical, electrophysiological, and/or electromechanical behavior of the heart. FEM is an effective tool for computational cardiac modeling applications that involve domains with complex geometry that are dynamic and changes as the heart beats. Moreover, FEM is also useful in accurately describing the anisotropic structure of the myocardial tissue that may influence the global function of the heart.

Current medical diagnostic practices lead to rough estimates of outcomes for a particular treatment. Most of these treatments and their results are based on clinical

trials. However, it is possible that these treatments may not directly apply to each patient as they are mostly based on averages. Hence, patient specific models can be used as an alternate diagnostic tool for treatment and therapy optimization. A lot of research is being done in developing patient specific computational models of blood vessels, bones, heart and the brain. Despite the advantages patient specific models offers, it is not widely used because their credibility is not widely tested owing to the number of manual steps that goes into making a model. Our aim in this project is to automate a few steps in the generation of cardiac geometry.

1.5 Finite Element Modeling of Cardiac Anatomy

Computational modeling is a powerful tool in integrating a pool of experimental information for understanding normal and abnormal cardiac function. Mathematical representation of the cardiac anatomy is a pivotal aspect in the process of using computational models for this integrative approach. Several finite element models of the ventricular geometry have been developed to date. Ventricular Geometry presented in this thesis was modeled in *Continuity 6.3* using a method similar to the mathematical representation developed by Nielson et al at the University of Auckland [6]. Three-dimensional hexahedral finite elements were used to model the geometry using prolate spheroidal coordinate system (λ, μ, θ). This heart model is a realistic representation of ventricular geometry. Prolate spheroidal coordinate system is chosen as it is a good initial approximation of the ventricular boundary geometry. It also requires fewer parameters to describe the elements compared to the rectangular cartesian coordinate. In addition, only the radial coordinate needs to be fitted. It is based on a finite element

reference topology describing the global geometry of the ventricular chambers. Linear polynomial interpolation of parameters at the element nodes are used to approximate the spatial variation of surface geometry within each element [51].

The coordinate system used in the governing equations for finite element modeling was general curvilinear coordinates (ξ_1, ξ_2, ξ_3) as shown in Figure 1-3 to efficiently model the cardiac anatomy [52].

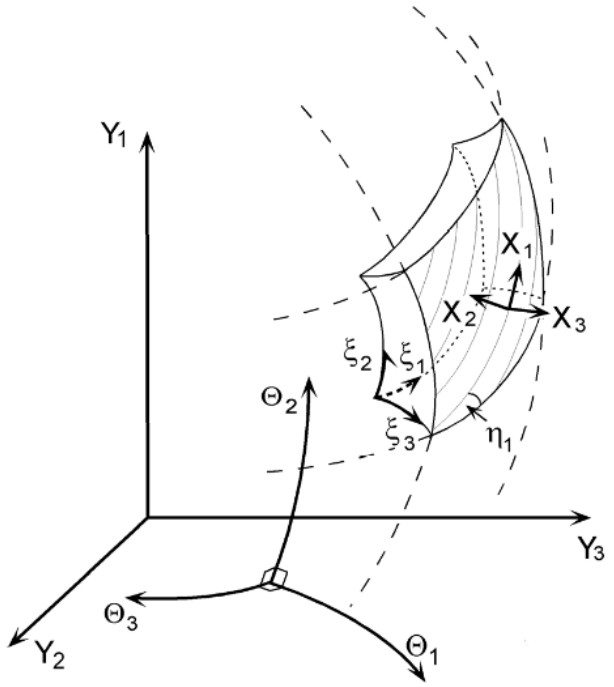

Figure 1-3: Figure showing the general curvilinear coordinates ((ξ_1, ξ_2, ξ_3). Source: Costa et al. (1996).

When constructing the 3D model, the radial coordinate λ is approximated using bicubic Hermite basis function in the (ξ_1, ξ_2) plane and a linear basis function in the ξ_3-direction. The angular coordinates, μ and θ, are approximated using trilinear Lagrange basis function. This approximation provides for sufficient degrees of freedom to model the complex ventricular surface geometry. Least squares fitting method was used to fit

the nodal parameters to ensure a realistic representation of the ventricular endocardial and epicardial surfaces. The model developed by Nielson et al had 24 3D elements and 41 nodes. This mathematical representation was used to model canine and rabbit hearts with data obtained from specially designed mechanical rig for the canine model [6] and digital imaging of the histological sections for the rabbit model [4].

Other groups have used these models to make modifications to the process of mesh generation. Trayanova et al used the rabbit biventricular model consisting of 36 linear-cubic Hermite hexahedral finite elements and 99 nodes to study cardiac defibrillation [58]. Finite element mesh for the study was generated by discretizing the six surfaces of the hexahedral elements into triangular elements. A volumetric tetrahedral mesh was generated for each of the 36 finite elements.

1.6 Image-based Cardiac Models

Image-based cardiac models have gained significant popularity due to advancement in imaging technology. High-resolution imaging data such as cardiac CT and MRI is now increasingly being used in developing anatomically realistic models of the heart. Finite element computational models are constructed using these imaging modalities by first discretizing the imaged objects [60]. The basic pipeline for model generation from medical imaging includes segmentation of the region of interest followed by finite element mesh generation. *Continuity 6.3* contains an image editing module which allows the user to perform segmentation and build a structured finite element mesh following the mathematical representation as described in the previous section. The imaging module in *Continuity* uses the iTK library (http://www.itk.org/)

with Python bindings to build level-set segmentation tools. This is used to create ventricular boundary data sets that are then mapped onto the nearest point on the surfaces of prolate spheroidal finite element meshes and fitted using the least-squares method.

More recently, other mesh generating algorithms have been developed like *Tarantula*, an Octree-based mesh generator that builds unstructured finite element meshes and is custom designed for cardiac modeling [53]. The algorithm, applied to segmented 3D image stacks, is fully automatic eliminating the need for user interaction. The underlying algorithm to develop an image-based unstructured mesh is described by Prassl et al [60]. The computational domain comprised of hybrid macroelements such as hexahedra, pyramids and prism. The shape functions used in building these finite element meshes are linear and piecewise continuous within each element. To perform simulations on these meshes, subtetrahedron meshes are required that are constructed by creating a virtual point at the center of each quadrilateral face. The entire volume mesh is then subject to final smoothing that required minimization of a nonlinear energy function for each cell locally. This method generates tetrahedral finite-element meshes representing complex geometries accurately with smooth surfaces. The resulting tetrahedral mesh had nodes and elements of the order of millions [60].

While the heart model developed by Nielson et al is simplified in that it excludes blood vessels, trabaculae and papillary muscles, the rabbit model described by Bishop et al at University of Oxford and Johns Hopkins University (JHU) [53] using *Tarantula* is more complex in that it includes the blood vessels and papillary muscles. However,

both of these models do not include important structural detail which is the Purkinje fiber network. A rabbit model used by Bishop et al was used for the simulation of electrical activation and compared to the structurally simple model. It was concluded that both the models showed similar electrical activation pattern, there were important differences in the activation sequence due to the level of anatomical details implemented. This rabbit model at JHU was constructed using high resolution MR imaging [53].

Another group at University of Texas at Austin has also published work on patient specific heart modeling using high resolution CT [56]. The computational pipeline used consisted of a series of steps including segmentation, noise filtering, differentiation of inner and outer surface boundaries, and volumetric decomposition of the heart and fitting initial surface mesh to an anatomically correct template of a 3D heart model. This method used high resolution CT images to construct the initial surface mesh after segmentation using *TightCocone* algorithm [57]. The resulting surface mesh is then matched and fitted to a template 3D model.

1.7 Ventricular Geometry

Ventricles are considered to be three-dimensional thick-walled pressure vessels. Through the course of the cardiac cycle, they show a high degree of variation in wall thickness and principal curvatures regionally and temporally. The ventricular walls are the thickest at the equator and base of the left ventricle in a normal heart. They are the thinnest at the left ventricular apex and right ventricular free wall. The left ventricle can be approximated by a thick ellipsoid of revolution truncated at the base. It is typically

defined by the major and minor radii of the left ventricular endocardium, left ventricular epicardium and right ventricular free wall. (Figure 1-4).

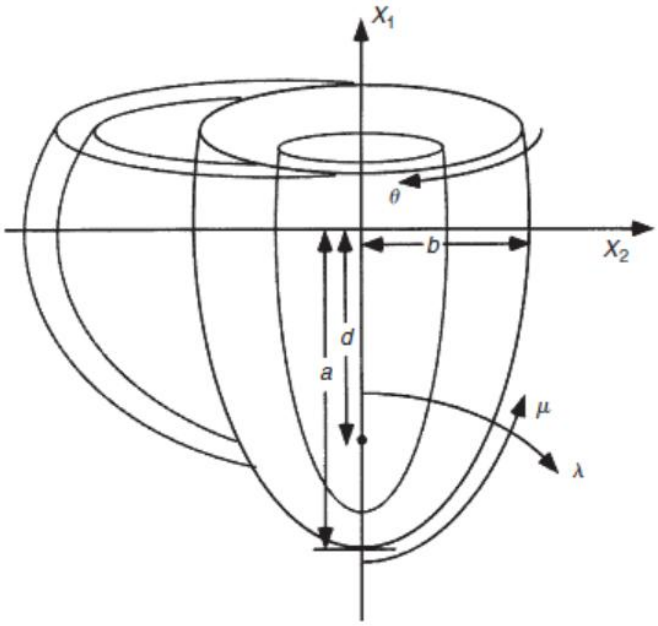

Figure 1-4: Ventricular geometry represented as a truncated ellipsoid. Figure shows major left ventricular radius (a), minor radius (b), focal length (d) and prolate spheroidal coordinates (λ, μ, θ). Source: McCulloch AD 2005 [3].

The position of the basal plane was defined by Streeter and Hanna [5] using a truncation factor f_b which was defined as the ratio of the longitudinal distances from equator-to-base and equator-to-apex. The total longitudinal distance extending from base to the apex is given by $(1+f_b)$ times the major radius of the ellipse. A constant value of 0.5 was used as f_b owing to small variation in f_b during systole and diastole in a canine model.

The focal length d of an ellipsoid is defined using the major (a) and minor radii (b) by

$$d^2 = a^2 - b^2 \quad \text{(Eqn 1.1)}$$

The focal length varies only slightly from the endocardium to the epicardium between end-diastole and end-systole. Due to the fact that the ventricular wall can be treated as ellipsoids of revolution, it can be assumed that the ellipsoids are confocal. This has led to the usage of prolate spheroidal coordinates (λ, μ, θ) system for characterizing ventricular geometries, for example, as obtained by noninvasive medical imaging [6, 7]. The relationship between cartesian coordinates (x_1, x_2, x_3) and prolate spheroid coordinates is given by

$$x_1 = d \cosh\lambda \cos\mu \quad \text{(Eqn 1.2)}$$

$$x_2 = d \sinh\lambda \sin\mu \cos\theta \quad \text{(Eqn 1.3)}$$

$$x_3 = d \sinh\lambda \sin\mu \cos\theta \quad \text{(Eqn 1.4)}$$

A constant transmural λ defines a surface which is an ellipse of revolution with major axis $a = d \cosh\lambda$ and minor axis $b = d \sinh\lambda$. The longitudinal coordinate μ varies from 0 at the apex to 120˚ at the base in an ellipsoidal model with a truncation factor of 0.5. The right ventricle wraps about 180˚ around the heart wall in the circumferential direction assuming a crescent-shape and extends about two-thirds distance from the base to apex longitudinally.

1.8 Goals

Over the years, detailed integrative models of coupled ventricular geometry and electromechanics have already been developed and validated for animal hearts but there is now a need for comparable models of the failing human heart. The goal of this study was to design an efficient methodology for developing three dimensional patient-

specific models of ventricular geometry in the failing *human* heart from clinical measurements such as 64-slice CT. In this thesis, detailed emphasis has been given to developing methods for semi-automatically generating three-dimensional cardiac geometry of heart failure patients from CT and MR images in *Continuity 6.3*. Methods developed for image segmentation, and three-dimensional finite element model development have been discussed in detail.

Both the patients studied in this thesis are HF patients with LBBB who have undergone BiV ICD implant. The ultimate goal would be to use patient-specific models built using such a methodology to predict and, possibly, optimize the outcomes of CRT. The overall workflow of the study is described in Figure 1-5.

Overall, the study is divided into three parts: clinical measurements (blue and green), models, model components or results (red), and validation of predictions from models (purple). The components highlighted in black are the focus for this thesis.

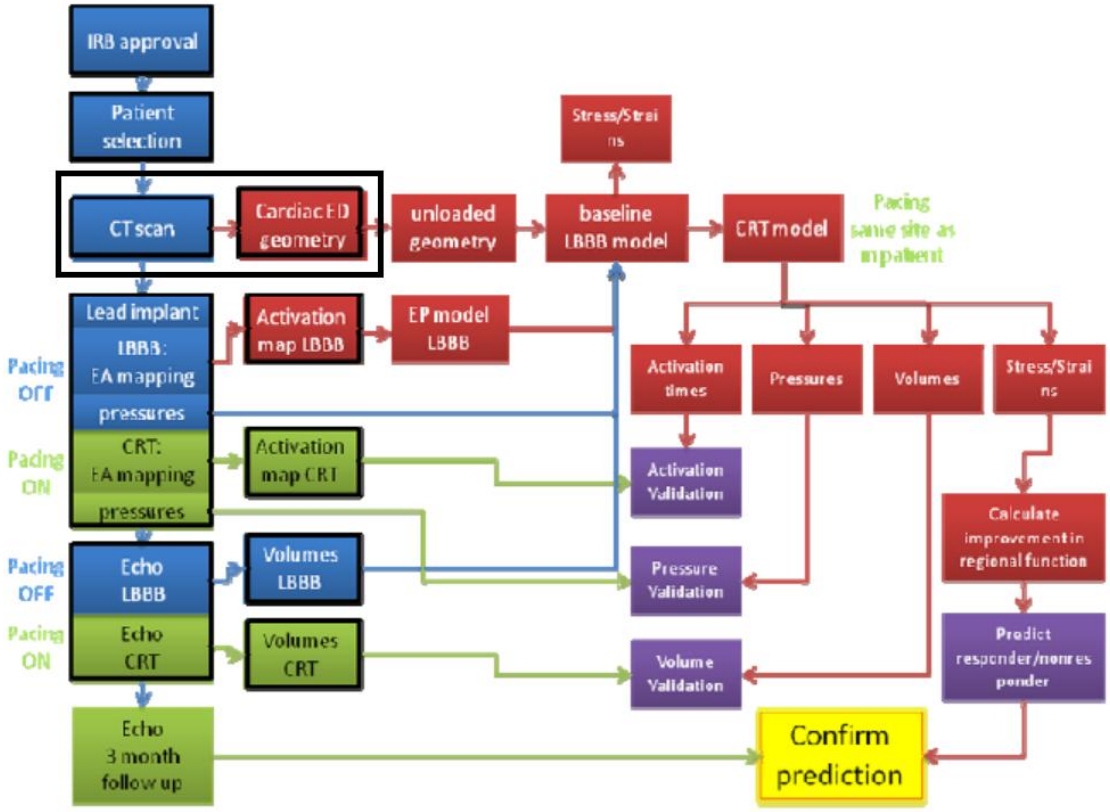

Figure 1-5: Workflow for design of patient-specific model to predict response to CRT. All baseline clinical measurements of LBBB are shown in blue; all measurements of CRT are shown in green and will be used for validation of the predictions made from patient-specific models. Shown in red are all models, components of models, or model results, and purple boxes show validations and predictions. Components highlighted in black are main focus of this thesis. Source: McCulloch 2008 [47].

2 Materials and Methods

2.1 Patient Selection and Bi-Ventricular Implantation

After receiving approval from the Institutional Review Board of the University of California and Veterans Affairs Medical Centers, San Diego, California, Dr. Sanjiv Narayan and Dr. David Krummen obtained data from patients with severe HF and left bundle branch block (which results in a wide QRS) from the VAMC. Informed consent was obtained by Dr. Krummen or Dr. Narayan from all the patients who were diagnosed enrolled in this study with NYHA class III or IV congestive heart failure. The presence of prior myocardial infarction (MI) was documented by electroanatomical mapping, but did not itself constitute as an exclusion criterion.

Two patient-specific models were built for the purpose of this thesis. The myocardial wall thickness calculation and volume estimation was performed on these

cardiac geometric models. Patient 1 in this study had a QRS width of 148ms and LVEF of 33.9%. Patient 2 had a QRS width of 162 ms and LVEF of 34.9%.

A biventricular Implantable Cardioverter Defibrillator (Bi-V ICD, St. Jude Medical, USA) was implanted in the patient with the left ventricular lead in a midlateral position. The right ventricular lead was implanted in the RV apex, and the right atrial (RA) lead in the right atrial appendage. Immediately following implantation, timing intervals (atrial to RV and RV to LV) were programmed as per the recommendations made by the QuickOpt Timing Cycle Optimization algorithm, which calculates appropriate atrioventricular (AV) delay settings based on the patient's intracardiac electrograms .

2.2 Clinical Measurements

2.2.1 Computed Tomography and Magnetic Resonance Imaging

Multi-slice helical CT scans of the patient were obtained before the BiV ICD implantation. The CT scanner used in this study was a GE Lightspeed 64-slice scanner (GE Healthcare Technologies, WI, USA). Prior to scanning, a bolus of non-ionic contrast agent (Omnipague 300, Amersham Health, Oslo, Norway) was injected through an antecubital vein at a rate of 5 mL/second. The patient was required to hold their breath for a brief time while the scanning was performed in the cranio-caudal direction at the level of the atrium with simultaneous acquisition of 64 sections per rotation (each section ~1.25mm), beam collimation of 10 mm, table speed of 16.75 mm/0.5 second (0.5 second tube rotation time, 120 kV, 310 mA). Contiguous axial CT

slices of thickness 1.25 mm were subsequently reconstructed and exported in DICOM format. The images were obtained at the end-diastole phase of the cardiac cycle.

For patient 2, Magnetic Resonance Imaging (MRI) was performed. Two-chamber short axis cine images were used for reconstruction. The slices had a pixel size of 1.4063 mm^2 and a slice thickness of 8mm. For each slice location, the first frame of the cine acquisition was used for segmentation of the ventricles and epicardium at end-diastole.

The CT and MRI images were then anonymized in DicomWorks to remove any patient identifying information for the purpose of research and protecting the identity of the patients.

2.3 Data Processing and Model Development

Three-dimensional models prove to be an efficient means to investigate how regional mechanics and electrical propagation depend on local properties. It is important to design efficient methods for fitting anatomic meshes that will accurately demonstrate the three-dimensional ventricular geometry which can be used to run various simulation to study the mechanical and electrical behavior of the failing heart.

Hunter and Smaill (1988) [50] outlined a continuum approach to build geometric models. Continuum models have to be appropriately represented for efficient and accurate computation. For this reason, finite element method (FEM) was used. The computational pipeline from 3D imaging to generating a computational model of cardiac geometry starting from CT or MRI scans of the heart consists of the following steps; (i) Image segmentation to extract the object of interest from images, (ii) selecting

landmark points or fiducial markers as anatomical locations on the segmented images, (iii) scaling the images based on the pixel size and slice thickness, (iv) image transformation that translates and rotates the data points to match the chosen model coordinate system, (v) converting the Cartesian coordinates to prolate spheroidal coordinates, (vi) interpolating all the nodes from landmark nodes to generate the initial mesh, (vii) two-dimensional fitting of the initial mesh to the data points from segmentation, and (viii) three-dimensional mesh construction by connecting the endocardial surfaces to the epicardium.

2.3.1 Image Segmentation

Image segmentation is the first step of the computational pipeline for mesh generation. It is fundamental in building a robust and spatially realistic 3D finite element model. Segmentation is a process of partitioning a digital image into multiple segments. It is basically used to simplify and dissect the features of interest from their surroundings. The result of segmentation is a set of surfaces developed as a result of the contours extracted from the image.

Image segmentation was carried out in the image editor contained in the fitting module of *Continuity 6.3*. Before the images could be imported into the image editor, the image stack was set to a dimension of 256x256. Figure 2-1 illustrates the steps followed in segmentation starting from the cardiac images. Since the CT and the MR images obtained are noisy and have low contrast, thresholding was used for contrast enhancement. Binary images were created from grayscale images. Manual thresholding method was used where the maximum and minimum pixel range for threshold was

manually adjusted in the image editor in *Continuity 6.3*. The value of the threshold is dependent on image brightness and was manually adjusted for every image used. Once a binary image was obtained, different regions were identified and labeled with different colors. Edge detection technique was used to identify the boundaries of the object of interest. Edge detection in image processing uses the sharp adjustment in intensity at the region boundaries. Label Edges tab was used in Continuity's image editor to perform edge detection.

For the construction of a biventricular cardiac geometry, four surfaces were extracted through segmentation – left and right ventricles and the epicardium (EPI). The right ventricle was further divided into the septum (ST) and the right ventricular free wall (RVFW). This is done to allow the independent fitting of these two surfaces. Therefore, the heart geometry consisted for LV endocardium, RVFW, ST and EPI. The data points obtained from edge detection were further processed to match the metric dimension of the actual images. The images were scaled in the x, y and z direction based on the pixel size for x and y direction and distance between the images for z direction.

Furthermore, the coordinate system used in CT and MR images is different from that used in Continuity. To develop a mathematical model in Continuity, a 'model' coordinate system is defined relative to the features of the heart. Owing to differences in anatomical features from heart to heart, standard features are used to define the axes. The x_1-axis of the model coordinate axis lied on the line connecting the LV apex and LV cavity centroid. The x_2-axis of the model coordinate system was located at the

bisection of the line from the RV cavity to septum. The image coordinate system was adjusted to the Continuity coordinate system through a series of rotations about an axis which will be discussed in the sections further.

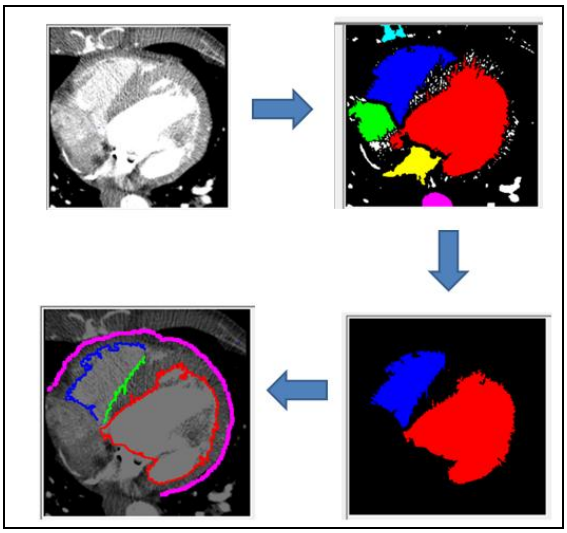

Figure 2-1: Cardiac images are converted to 256 x 256 bitmap format (top left) before importing into Continuity image editor. Thresholding is performed and color labels are used to label different components (top right). Components of interest are selected (bottom right) by changing the labels of other components to black and edge detection (bottom left) is used to mark the boundaries.

After scaling and segmentation were performed, image masks depicting the four surfaces were obtained.

2.3.2 Landmark Points

A new method for generating initial mesh was developed. This method makes use of landmark points that act as fiducial markers. Landmarks points are anatomical locations on the heart and are identified on the segmented images. The coordinates of these points are used to build the initial mesh. In order to make a biventricular model

of cardiac geometry, seventeen landmark points were used with twelve points at the base and five points at the apex. The criteria for choosing these points was to enable the use of a minimum number of markers that define the lateral, posterior, mid-septal and anterior position of each surface at the base. Apical points were chosen so as to determine the length of the heart. Basal and apical landmarks provide an adequate estimate of the circumferential and longitudinal extent of the heart. These points were also selected so as to allow automatic image transformation which will be discussed in detail later in this chapter.

The landmark points used were- LV midseptal basal endocardium, LV anterior basal endocardium , LV lateral basal endocardium, LV posterior basal endocardium , RV midseptal basal endocardium, RV lateral basal endocardium, RV anterior basal endocardium, RV posterior basal endocardium, RV lateral basal epicardium, RV anterior basal epicardium, LV lateral basal epicardium, RV posterior basal epicardium, RV midseptal apical endocardium, RV anterior apical endocardium, RV posterior apical endocardium, LV apical endocardium, LV apical epicardium . Appendix A shows the seventeen landmark points identified on cardiac CT images for patient 1.

2.3.3 Image Transformation

The CT and the MRI images obtained from the patient need to be transformed in order to build a cardiac model. Image transformation involves two steps; (i) Translation and (ii) Rotation. Translation is a way to move the image or data points horizontally and/or vertically. Translation is a helpful technique to adjust the origin of the model coordinate system. An automated method was implemented into *Continuity 6.3* to

perform image transformation using three landmark points. This enabled the translation of the data points and the landmark points to change the axes from CT coordinates to Continuity's coordinates. The data points were translated prior to rotation. The origin of the model coordinate system lies at two-thirds apex to base. The origin was calculated as one-third the sum of three vectors:

$$Origin = \frac{1}{3}(I^1 + I^2 + I^3) \quad \text{(Eqn 2.1)}$$

where I^1=LV midseptal basal endocardium, I^2=LV lateral basal endocardium, I^3=LV apical endocardium. After the data points were translated to adjust the origin, rotation was performed.

Rotation is a transformation in a plane or in space that describes the motion of a rigid body around a fixed point in two-dimension and around a fixed axis in three-dimension. It is critical to know the frame of reference when considering rotations, since all rotations are described relative to a particular frame of reference. When an orthogonal transformation is performed on a body in any coordinate system, there exists an inverse transformation which results in the body being at the original coordinates when applied to the frame of reference. Vector rotation was performed using RX=Y, where R is the rotation matrix, X represents the initial coordinates and Y the final coordinates. Algebraically, a rotation matrix is orthogonal which means $R^T=R^{-1}$ with determinant equal to 1. Three landmark point coordinates – LV apical endocardium, RV midseptal basal endocardium and RV midseptal apical endocardium – prior to rotation − were used to derive initial axis of the data points. The rotation matrix consisted of

normal unit vectors derived from three landmark points. The rotation matrix was as follows:

$$R = [\overrightarrow{e_{(1)}}, \overrightarrow{e_{(2)}}, \overrightarrow{e_{(3)}}] \quad \text{(Eqn 2.2)}$$

The vector $\overrightarrow{e_{(1)}}$ points from the origin to the LV apical endocardium (Z^1).

$$\overrightarrow{e_{(1)}} = \frac{Z^1}{|Z^1|} \quad \text{(Eqn 2.3)}$$

The vector $\overrightarrow{e_{(2)}}$ points from the origin to the RV mid-septal endocardium. Since the vector $\overrightarrow{e_{(2)}}$ is not necessarily perpendicular to the vector $\overrightarrow{e_{(1)}}$, parameterization of the RVFW curve was done to get a point that was perpendicular to vector $\overrightarrow{e_{(1)}}$. Parameterization is the process of defining the parameters required for a complete or relevant specification of a model or geometry. This may involve one or more parameters that are variables. In general, these parameters influence the shape of the curve in a way which is more complicated that a simple linear transformation. The vector $\overrightarrow{e_{(2)}}$ is given in terms of the parameterized equation as follows:

$$\overrightarrow{e_{(2)}} = \frac{p}{|p|} \quad \text{(Eqn 2.4)}$$

The parameterized equation consists of a variable α and two landmark points on the RV curve- RV mid-septal basal endocardium and RV mid-septal apical endocardium and is given by:

$$p = (1-\alpha)z^5 + \alpha z^{13} \quad \text{(Eqn 2.5)}$$

where the variable α is given by

$$\alpha = \frac{z_1^5\overrightarrow{e_{(1)1}} + z_2^5\overrightarrow{e_{(1)2}} + z_3^5\overrightarrow{e_{(1)3}}}{(z_1^5 - z_1^{13})\overrightarrow{e_{(1)1}} + (z_2^5 - z_2^{13})\overrightarrow{e_{(1)2}} + (z_3^5 - z_3^{13})\overrightarrow{e_{(1)3}}} \quad \text{(Eqn 2.6)}$$

where *p*=parameterized equation to find the perpendicular point, z^5= the 3D coordinates of the RV midseptal basal endocardium point , and z^{13}= the 3D coordinates of the RV midseptal apical endocardium point. Vector $\overrightarrow{e_{(3)}}$ was taken as the cross product of vector $\overrightarrow{e_{(1)}}$ and $\overrightarrow{e_{(2)}}$. The rotation matrix was used to compute the axis and angle about which this rotation occurred based on Euler's rotation theorem. Rotation about a given axis and angle can be represented by the following rotation matrix [20]:

$$r = \begin{bmatrix} u_x^2 + (1-u_x^2)c & u_x u_y(1-c) - u_z s & u_x u_z(1-c) + u_y s \\ u_x u_y(1-c) + u_z s & u_y^2 + (1-u_y^2)c & u_y u_z(1-c) - u_x s \\ u_x u_z(1-c) - u_y s & u_y u_z(1-c) + u_x s & u_z^2 + (1-u_z^2)c \end{bmatrix} \quad \text{(Eqn 2.7)}$$

where $c = \cos\theta$ and $s = \sin\theta$. Comparing this matrix to the rotation matrix *R* derived from the normal unit vectors, axis and angle of rotation are computed.

$$u_x = \frac{R_{32} - R_{23}}{2\sin\theta} \quad \text{(Eqn 2.8)}$$

$$u_y = \frac{-(R_{31} - R_{13})}{2\sin\theta} \quad \text{(Eqn 2.9)}$$

$$u_z = \frac{R_{21} - R_{12}}{2\sin\theta}, \quad \text{(Eqn 2.10)}$$

$$\theta = \cos^{-1}\left[\frac{R_{11} + R_{22} + R_{33} - 1}{2}\right] \quad \text{(Eqn 2.11)}$$

The data points and the landmark points are then multiplied by the rotation matrix to align the points to meet the requirements of the model coordinate system.

2.3.4 Rectangular Cartesian to Prolate Spheroidal Coordinates

The data points and landmark nodes obtained after segmentation are in rectangular cartesian coordinates (*x*, *y*, *z*). These need to be converted into prolate

spheroidal coordinates given in terms of (λ, μ, θ). The left ventricular endocardial and epicardial boundaries are treated as ellipses of revolution and the resulting ellipsoids are assumed to be confocal. Therefore, prolate spheroidal coordinates are chosen to represent the ventricular geometry. The radial coordinate λ is a non-negative real number and $\mu \in [0, \pi]$ is the longitudinal coordinate. The circumferential coordinate is represented by the angle θ and belongs to the interval [0, 2π). Equations 1.2, 1.3 and 1.4 can be used to convert prolate spheroidal coordinates to rectangular Cartesian coordinates. These equations are modified in a way to convert cartesian to prolate spheroidal coordinates. Appendix B shows the m-file used for the conversion. Using equation 1.3 and 1.4, θ coordinate can be computed.

$$\theta = \tan^{-1}\frac{x_3}{x_2} \quad \text{(Eqn 2.12)}$$

A series of algebraic steps are carried out to derive λ and θ. Using the trigonometric identities (equation 2.13 and 2.14), λ can be computed.

$$\frac{x_1^2}{d^2 cosh^2\lambda} + \frac{x_2^2 + x_3^2}{d^2 sinh^2\lambda} = 1 \quad \text{(Eqn 2.13)}$$

$$cosh^2\lambda - sinh^2\lambda = 1 \quad \text{(Eqn 2.14)}$$

Defining a variable m, the above equation can be reduced a quadratic equation.

$$m = cosh^2\lambda \quad \text{(Eqn 2.15)}$$

Substituting m in equation 2.13,

$$\frac{x_1^2}{d^2 m} + \frac{x_2^2 + x_3^2}{d^2(m-1)} = 1 \quad \text{(Eqn 2.16)}$$

Rearranging equation 2.16,

$$\frac{x_1^2 + x_2^2 + x_3^2}{d^2} + 1 = m + \frac{x_1^2}{d^2 m} \quad \text{(Eqn 2.17)}$$

Defining two constants c_1 and c_2, equation 2.17 can be re-written as a quadratic equation

$$m^2 - c_1 m + c_2 = 0 \quad \text{(Eqn 2.18)}$$

where, $c_1 = \frac{x_1^2 + x_2^2 + x_3^2}{d^2} + 1$ (Eqn 2.19)

$$c_2 = \frac{x_1^2}{d^2} \quad \text{(Eqn 2.20)}$$

The λ coordinate can be computed in terms of *m* and equation 2.21

$$\cosh^{-1} x = \ln(x + \sqrt{x^2 - 1}), \qquad x > 1 \quad \text{(Eqn 2.21)}$$

$$\lambda = \ln(\sqrt{m} + \sqrt{m-1}), \qquad \sqrt{m} > 1 \quad \text{(Eqn 2.22)}$$

Similarly, using a trigonometric identity (equation 2.23), μ can be computed.

$$\frac{x_1^2}{d^2 cos^2 \mu} - \frac{x_2^2 + x_3^2}{d^2 sin^2 \mu} = 1 \quad \text{(Eqn 2.23)}$$

$$n = cos^2 \mu \quad \text{(Eqn 2.24)}$$

$$\mu = \cos^{-1} n, \qquad n \leq 1 \quad \text{(Eqn 2.25)}$$

2.3.5 Initial Finite Element Mesh Set up

It is important to create a finite element surface model that closely resembles the geometry of the heart. The initial finite element surface model consisted of two

truncated ellipsoids for LV and EPI and two-semi-spheroidal surfaces for ST and RVFW. It is necessary to have sufficient number of nodes and elements to allow for enough degrees of freedom to achieve accurate fitting results. A simple initial mesh was constructed with 50 nodes and 40 two-dimensional elements- 4 circumferential and 3 longitudinal elements for LV, ST and EPI and 2 circumferential elements RVFW (Figure 2-2). Since RVFW extends two-thirds from the base, it had 2 longitudinal elements. The focal length of the ellipsoid was also calculated based on landmark points using equation 1.1. The major axis was defined as the vector pointing from the origin to LV apical endocardium and the minor axis was defined as the vector pointing from the origin to RV mid-septal basal endocardium.

The coordinates of all the 50 nodes were derived from the 17 landmark points identified on the images. Prolate spheroidal coordinates of the landmark points were used to interpolate the remaining nodes. The μ value of the nodes at the base and the apex were based on the landmark points and were approximately at 120° and 0° respectively owing to the origin being at two-thirds from the apex to base (Figure 2-3). Appendix C shows the python script containing the equations used for the interpolation of all the 50 nodes from seventeen landmark points. The initial mesh was converted from bilinear Lagrange to bicubic Hermite basis function. Figure 2-4 shows the initial mesh and the data points derived from segmentation. While Figure 2-2, 2-3, and 2-4 illustrates the initial mesh developed for patient 1, Figure 2-5 and 2-6 illustrates the initial mesh developed for patient 2.

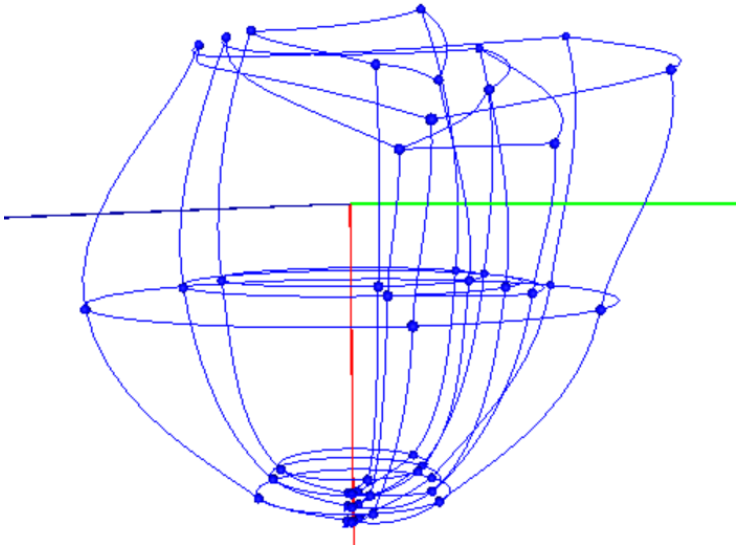

Figure 2-2: Posterior view of the initial mesh (Patient 1) developed from the 17 landmark points

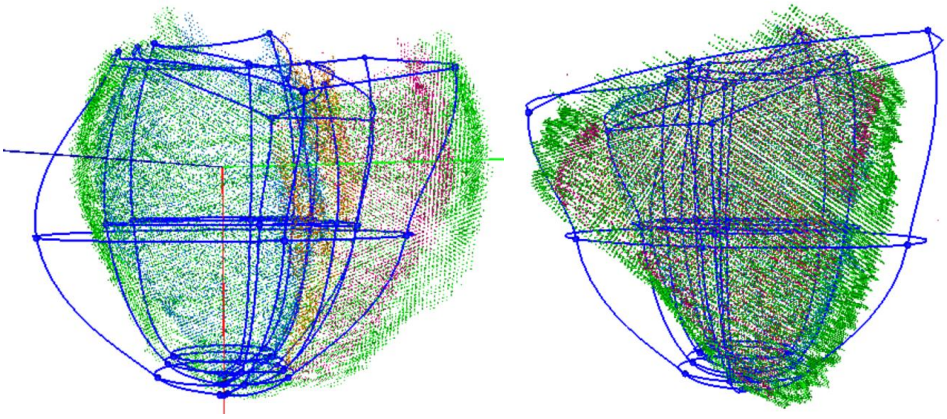

Figure 2-3: Posterior view of the initial mesh (Left) with data points and anterior view of the initial mesh (Right) with data points from segmentation showing the axes; x-axis (red), y-axis (green) and z-axis (blue) of the model coordinate with origin being at one-thirds from base to apex

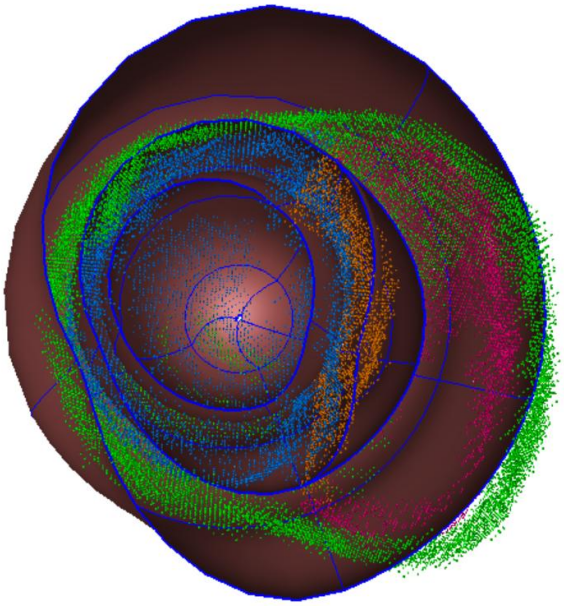

Figure 2-4: Posterior top view of the initial mesh developed for patient 2 showing the data points derived from segmentation.

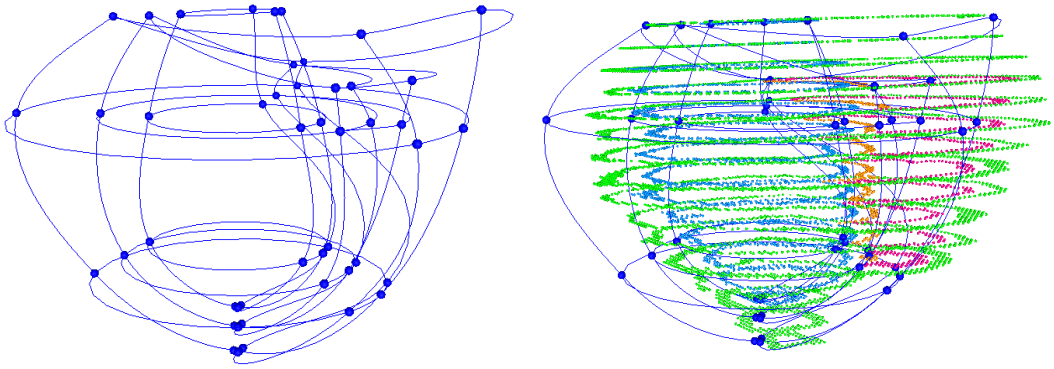

Figure 2-5: Posterior view of the initial mesh (left) with data points (right) for patient 2.

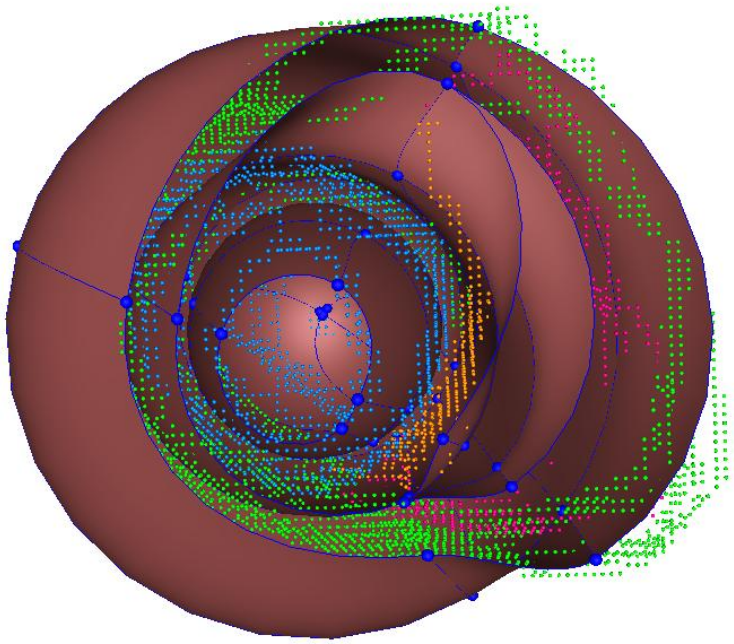

Figure 2-6: Posterior top view of the initial mesh for patient 2 showing data points from segmentation.

2.3.6 Two-dimensional Mesh Fitting

The two-dimensional initial mesh was then fitted to the data points obtained from segmentation. The nodal coordinate parameters of bicubic hermite finite element meshes for all the four surfaces- LV, EPI, ST, and RVFW were fitted using the linear least-squares method. An advantage of using the prolate spheroidal coordinate system is that it requires fitting in only λ coordinate. Several constraints were imposed on the fit to ensure derivative symmetry at the LV, EPI, ST and RVFW apex. The values of the λ coordinate of LV and EPI apex were coupled by 1 indicating that they are the same node. The derivatives of the LV and EPI nodes at the apex were set such that there is no movement of the nodes during fitting. Constraints were also imposed on the nodes at

RVFW junction to keep in place while fitting. All the midnodes of the ST were set to be mid way between the LV and EPI nodes.

Least Squares Fitting of Nodal Parameters

Using the linear least-squares fitting algorithm in *Continuity 6.3*, an initial finite element mesh can be fitted to the data points by applying appropriate constraints in order to produce a realistic geometric model. The linear least squares fit is obtained by minimizing the objective function.

$$F(\mathbf{X}) = \sum_{d=1,D} \gamma_d \left\| \mathbf{X}(\zeta_d) - \mathbf{X}_d \right\|^2 + \int_\Omega \left\{ \alpha \left(\left\| \frac{\partial \mathbf{u}}{\partial \zeta_1} \right\|^2 + \left\| \frac{\partial \mathbf{u}}{\partial \zeta_2} \right\|^2 \right) + \beta \left(\left\| \frac{\partial^2 \mathbf{u}}{\partial \zeta_1^2} \right\|^2 + \left\| \frac{\partial^2 \mathbf{u}}{\partial \zeta_2^2} \right\|^2 \right) + \alpha^2 \left\| \frac{\partial^2 \mathbf{u}}{\partial \zeta_1 \partial \zeta_2} \right\|^2 \right\} d\zeta \quad \text{(Eqn 2.26)}$$

where $\mathbf{X}_d$ is the coordinate of the data point and $\mathbf{X}(\xi_d)$ is the interpolated value of the projection of the measured point onto the surface of element along the λ axis. α and β are the fitting weights associated with the smoothing function and γ_d is the smoothing weight given to each data point. The first term minimizes the error between the coordinate of each data point and the corresponding coordinate of the projection on the surface of the element along the λ axis. The term γ_d was set to one assuming all measurements were equally accurate. The second term is associated with the amount of stretch or the first derivative terms and bending or the second derivative terms. It does so by penalizing the terms of the difference component field $u=X-X^0$, where X^0 is the initial estimated epicardial surface. The terms α and β are critical as they determine the smoothness of the geometric fit.

2.3.7 Three-dimensional Mesh Generation

The two-dimensional fitted mesh is composed of a set of two-dimensional elements that consists of 4 nodes. The two-dimensional fitted surfaces are then connected together to form a three-dimensional mesh. Three-dimensional elements are defined by 8 nodes. The basis functions that define the mesh were changed from bicubic Hermite to bicubic-linear Hermite in the λ direction and from bilinear Lagrange to trilinear Lagrange in μ and θ directions. The basis functions allows for the calculation of new derivatives that lead to smooth connections between each element.

2.4 Myocardial Thickness Estimation

The three-dimensional end-diastolic biventricular model of the heart was used to calculate end-diastolic myocardial wall thickness. Septal wall thickness (SWT) and LV free wall thickness were calculated for each of the three patients enrolled in the study. The images used for reconstruction were short axis cine images. To calculate the myocardial wall thickness from the 3D model of the heart, perpendicular distance was measured from the epicardium to the endocardium. A number of nodal coordinates were interpolated from the 3D model using *Continuity 6.3*. Cartesian coordinates of these points were used to map the endocardial nodes to the epicardial nodes at the same longitudinal and circumferential level in order to calculate the perpendicular distance between the points. This distance was averaged over the LV free wall region of the heart to calculate the LV free wall thickness and over the septal region to calculate the septal wall thickness.

2.5 Ventricular Cavity and Myocardial Volume Estimation

The 3D model of the heart was used to estimate the ventricular cavity and myocardial volume in each of the three patients using *Continuity 6.3*. In order to calculate the volume, an origin was specified at the base of the heart. Endocardial and epicardial volumes were obtained by summing the volumes of pyramids that are made up by endocardial and epicardial faces and the origin of the ventricular base. The volume of a pyramid is calculated using the formula $V = (1/3)*B*h$ where B is the area of the base of the pyramid (here surface integral of the area of the endocardial or epicardial face of an element) and h is the perpendicular distance between the origin and the endocardial and epicardial element face. Myocardial wall volume is calculated as the difference between epicardial and endocardial cavity.

The volumes obtained from the 3D model were validated by calculating the LV cavity volumes from the CT and MRI data using Simpson's method. LV Endocardial contours from segmentation of the CT and MR images were imported into *ImageJ* to calculate the cross-sectional area. LV cavity volumes were calculated by multiplying the cross-sectional area by the slice thickness.

$$V = \sum_{i=1}^{n} A_i \times d \qquad \text{(Eqn 2.27)}$$

where A_i= cross-sectional area of each slice

d= slice thickness

n= number of slices

3 Results

3.1 Image Segmentation

Short-axis cine CT and MR images at end-diastole were segmented. The voxel size of the CT images used for scaling was 0.488mm x 0.488mm x 1.25mm and that used for MR images was 1.12mm x 1.12mm x 8mm. The resolution of MR images was scaled to change the original resolution of 1.406mm x 1.406mm x 8mm match the cropped imaged used for segmentation. The contiguous axial CT slices obtained from the multislice CT scanner were then segmented in *Continuity 6.3*. Figure 3-1 shows the stack of image slices obtained from CT. Figure 3-2 shows the ventricles segmented from these CT slices. Once segmentation was performed, the data points were rendered that resembled the structure of the ventricles in human heart (Figure 3-3). This procedure was repeated for MR images for patient 2.

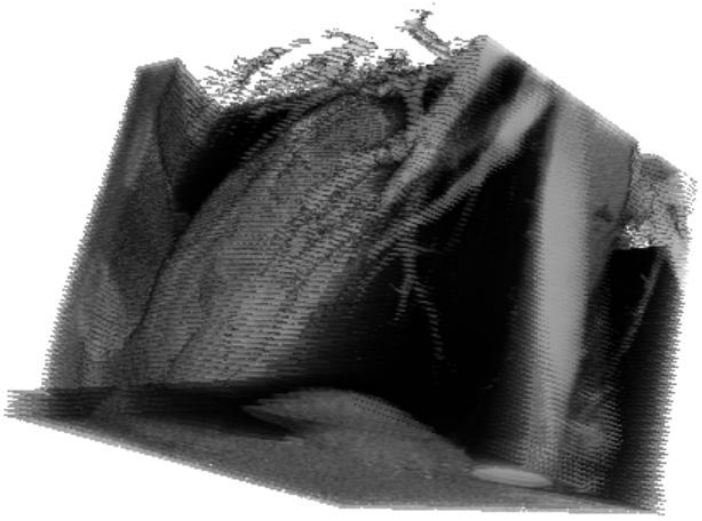

Figure 3-1: Stack of images obtained from CT

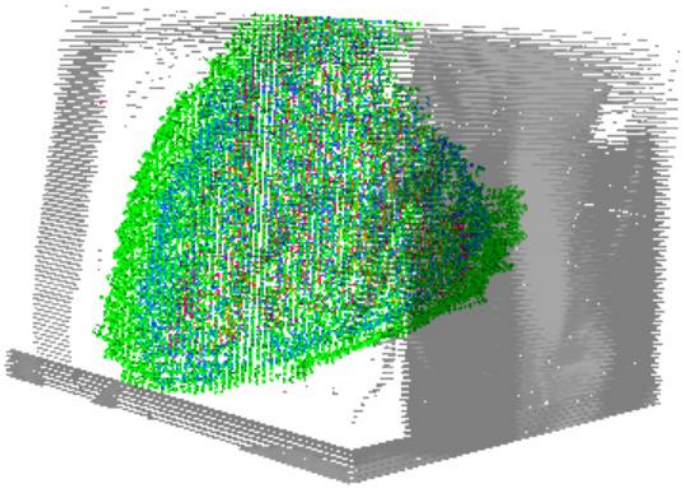

Figure 3-2: Stack of images showing the segmented endocardium and epicardium

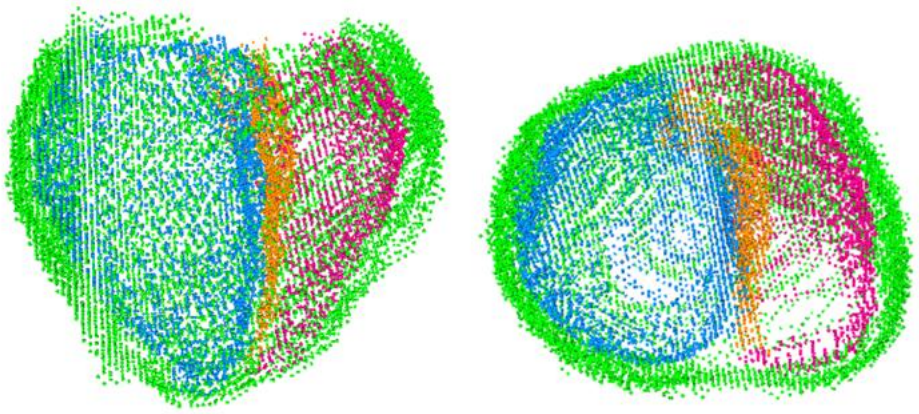

Figure 3-3: Data points showing the posterior view (left) and the top view (right) of the human heart.

3.1 Landmark Points

Segmented images were imported into the imaging module of *Continuity 6.3* and landmark points were identified (Figure 3-4). Seventeen landmark points were identified (Figure 3-5). Appendix A gives a detailed overview of all the seventeen landmark points.

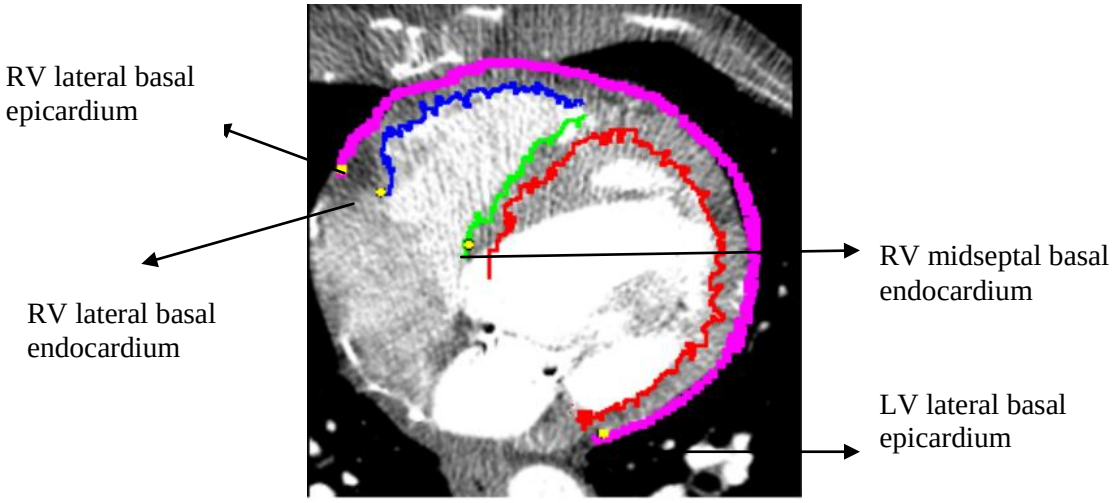

Figure 3-4: CT slice showing segmented contours and four of seventeen landmark points. Pink contour represents the epicardium, red represents the LV endocardium, blue represents RVFW and green represents ST wall.

Figure 3-5: Spatial distribution of all the seventeen landmark points (left) with five points at the apex (center) and twelve points at the base (right).

3.2 Image transformation and Model Development

Using the coordinates of the landmark points, the original data points were translated to position the origin at two-thirds from apex to base. Since the CT and MRI coordinates (Figure 3-6) are different from the model coordinate system, data points had to be rotated to align the *x*-axis along the long axis of the heart and the *y*-axis bisecting the septal wall (Figure 3-7).

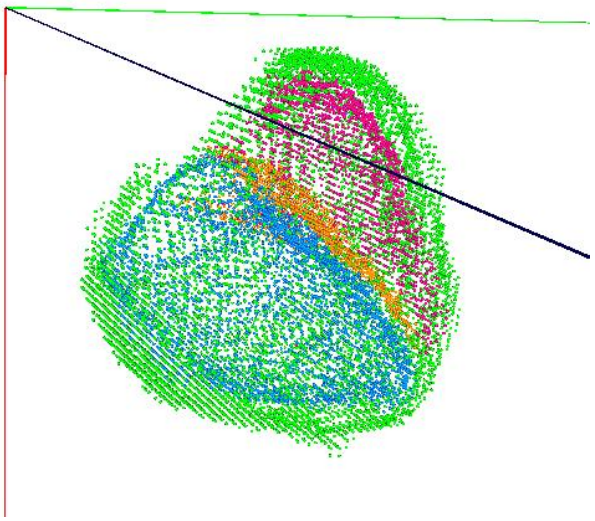

Figure 3-6: Data points aligned according to the CT coordinate system for patient 1.

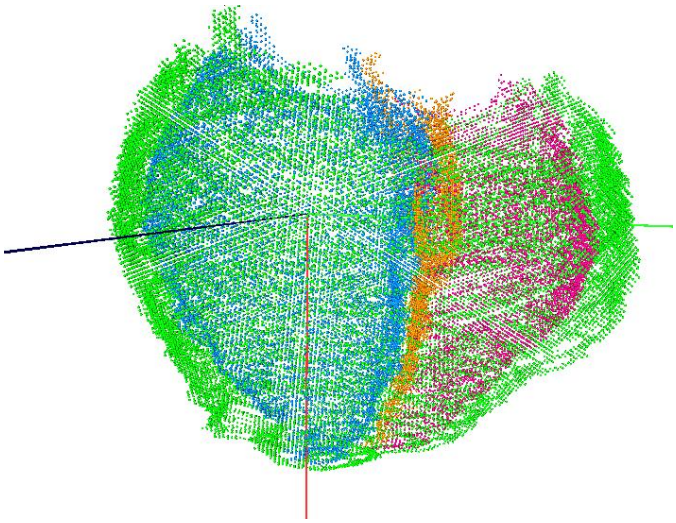

Figure 3-7: Data points translated to adjust the origin at two-thirds from apex to base and rotated to align the x-axis (red) along the long axis of the heart and the y-axis bisecting the septum and RVFW.

A geometric model of the heart at end-diastole was created using prolate spheroidal bi-cubic Hermite finite element surface meshes which were fit to endocardial and epicardial boundary points. The fit was performed using a least squares minimization of the λ coordinate with bicubic Hermite interpolation. In order to

generate a mesh comprising of 50 nodes and 40 elements from 17 landmark points, more nodes were created by interpolation between landmark points. Two patient-specific failing heart geometries were modeled. The initial mesh was fitted to the data points from segmentation (Figure 3-8, Figure 3-9). For the first heart, smoothing weights ranging from 0 to 0.001 were used to fit the surfaces. A smoothing weight of 0.01 was used to fit the LV and EPI surfaces while a smoothing weight of 0.05 was used to fit the ST and RVFW. These values of the smoothing weights resulted in the best fit model with an average RMS error of 0.065. Only the radial coordinate was fit. Hence, the RMS error represents the error in the λ coordinate. One of the ways of interpreting this error is considering if the average λ value of the epicardial surface is 0.788, then an average RMS error of 0.065 means there is a possibility of a variation of 8.24%. Also, with an error of 0.065, the variation in the length of major and minor axis for a model with focal length of 54 mm is 6.72 mm and 3.04 mm respectively. The resulting 2D mesh had smooth surfaces that realistically represented the geometry of the failing heart (Figure 3-10).

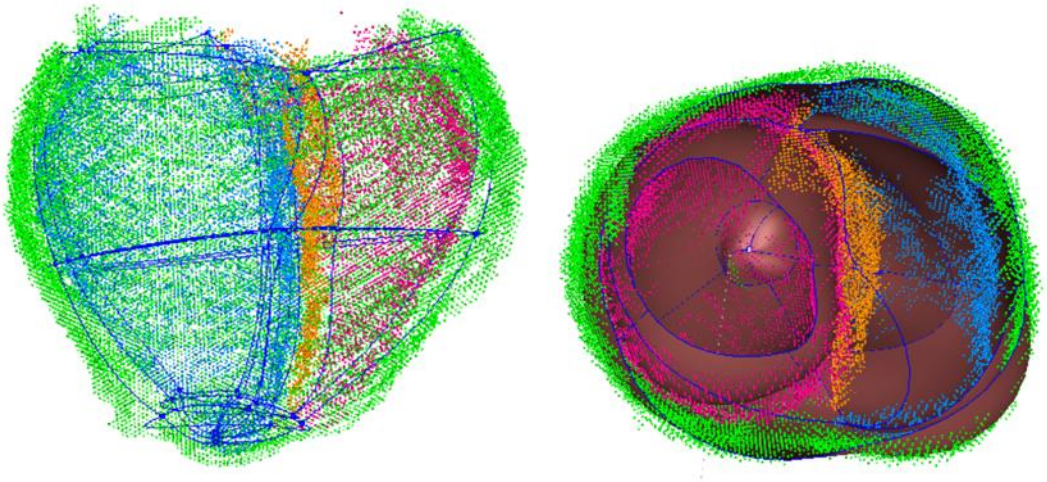

Figure 3-8: Posterior view of the fitted mesh (Left) and top posterior view of the fitted mesh (right) with data points for patient 1.

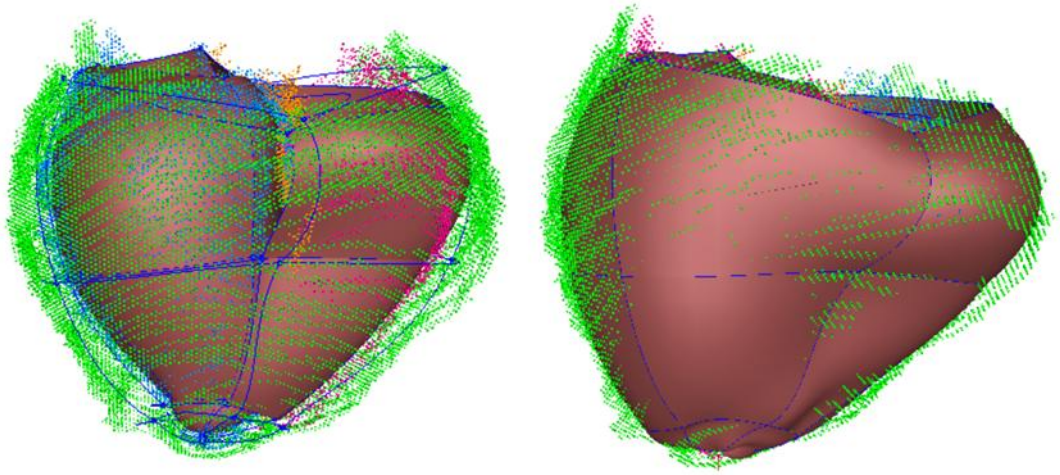

Figure 3-9: Fitted endocardium (left) and fitted epicardium (right) with data points for patient 1.

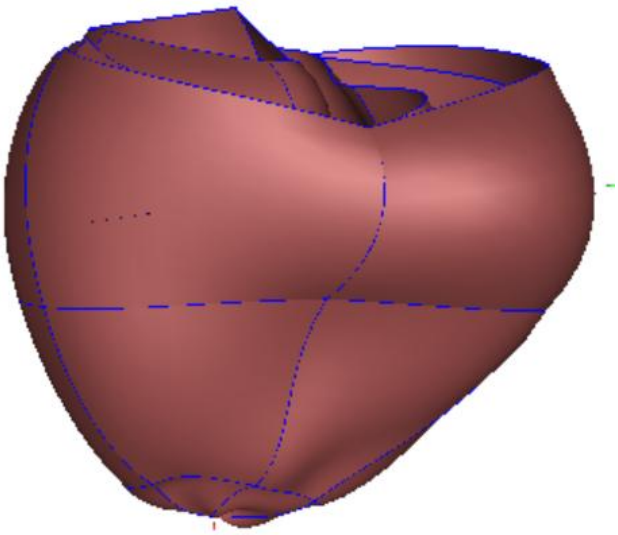

Figure 3-10: Biventricular patient-specific model of the failing heart of patient 1.

The 3D cardiac geometrical model was derived from the 2D mesh by changing the basis function. The 2D elements were then converted into 3D elements (Figures 3-11 and 3-12).

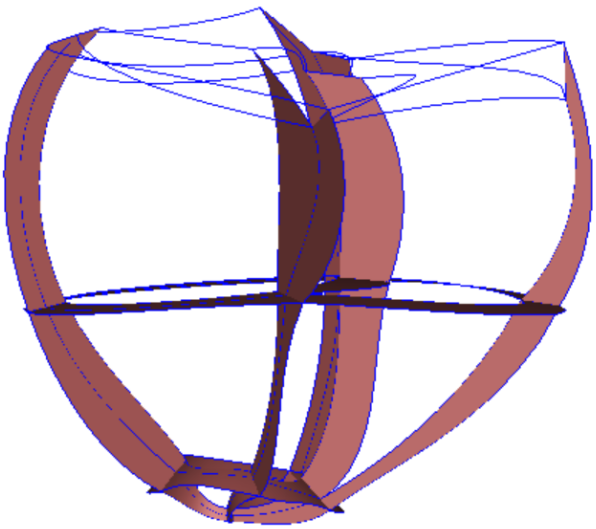

Figure 3-11: Three-dimensional model of the human heart (patient 1) showing the $x_i(1)$ and $x_i(2)$ coordinates.

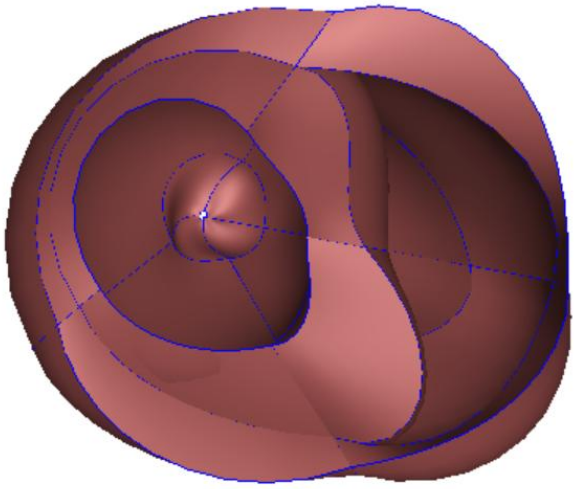

Figure 3-12: Top posterior view of the three-dimensional patient-specific model of human heart (patient 1).

The second patient model (Figures 3-13 and 3-14) was generated from MRI images following the same procedure as for the CT images. Smoothing weights ranging from 0 to 0.001 were used to get the best fit geometry of the failing heart. A smoothing weight of 0.05 was used to fit the LV and EPI surfaces smoothly and 0.1 was used to fit RVFW and ST (Figure 3-15). The resulting 2D mesh accurately represented the geometry of the heart for this patient based upon the average RMS error in the radial direction which was 0.083. An average RMS error of 0.083 means there is a possibility of a variation of 8.82% for average λ value of 0.941 on the epicardial surface. Also, with an error of 0.083, the variation in the length of major and minor axis for a model with focal length of 64 mm is 4.13 mm and 8.28 mm respectively. The 2D mesh was then converted to 3D mesh (Figure 3-16).

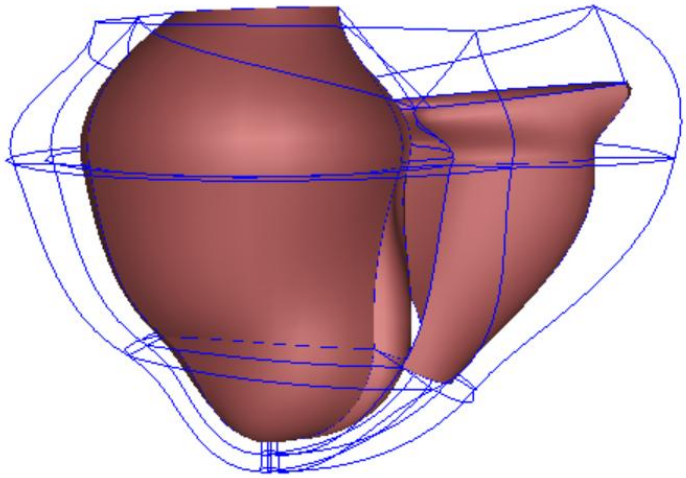

Figure 3-13: Fitted patient-specific model showing endocardial surfaces of the failing heart of patient 2.

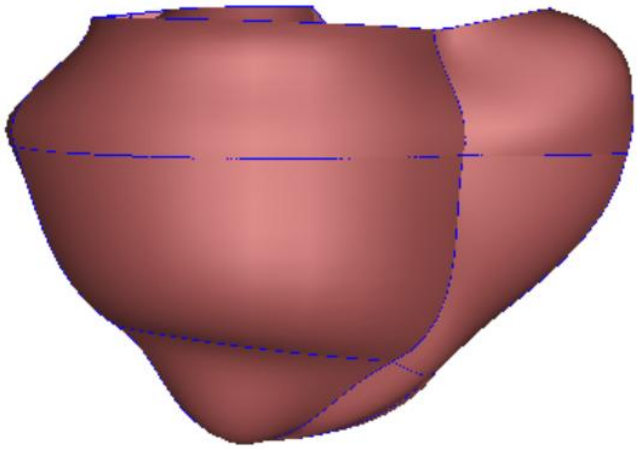

Figure 3-14: Fitted patient-specific model showing epicardial surface of failing heart of patient 2.

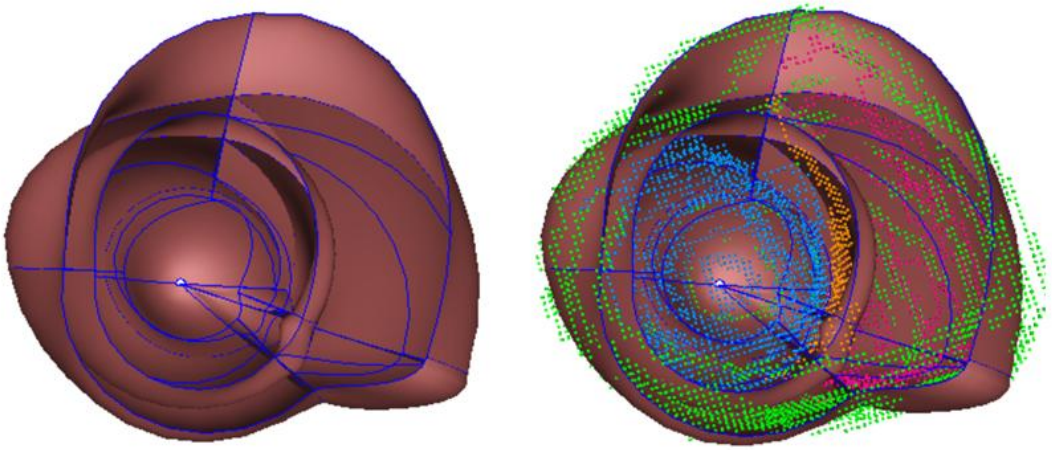

Figure 3-15: Posterior top view of the fitted model (left) showing data points (right) obtained from segmentation of MR images of patient 2.

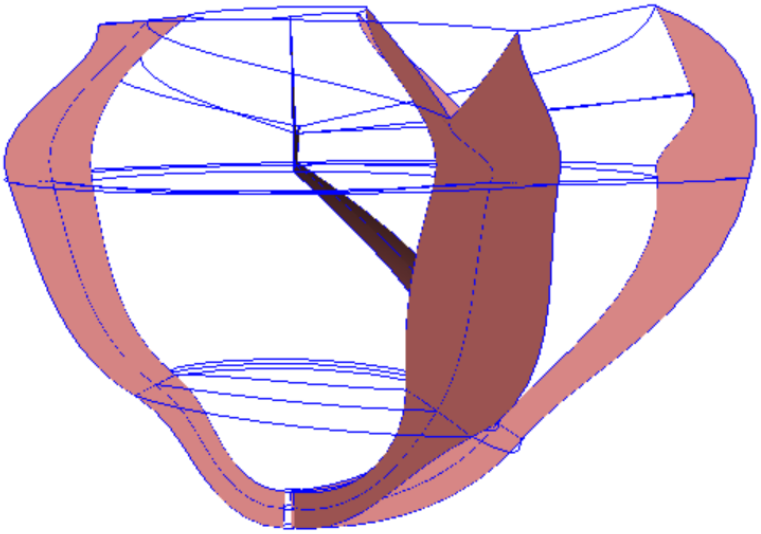

Figure 3-16: 3D model showing $x_i(1)$ and $x_i(2)$ surfaces of the failing heart of patient 2.

3.3 Myocardial Wall Thickness Estimation

Myocardial wall thickness was measured in three patient specific models. All the three models represent dyssnchronous heart failure. The models developed in this study were end-diastolic loaded geometrical models.

The table 3.1 below shows the end-diastolic septal wall thickness (EDSWT) and end-diastolic LV Free wall thickness (ED-LVFWT) for the two HF patients. Also shown are the thicknesses measured using 2D transthoracic Echocardiograms of the patient's heart recorded in real-time at 33 frames per second at the VAMC.

Table 3-1- Table comparing the SWT and PWT calculated using 3D Model and Echocardiograms

	SWT (cm)	**SWT(Echo- cm)**	**LV Free Wall (cm)**	**LV Free Wall (Echo-cm)**
Patient 1	0.93	1.1	0.78	0.6
Patient 2	1.24	1.5	1.26	1.3

Ventricular wall thickness is also presented on a standard called 'Bull's eye' plots. A bull's eye is a 2D plot which is divided into 17 sectors. It provides an intuitive overview of the viability of the entire left ventricular myocardium in a single diagram. The outer ring in the plot represents the base, the middle ring represents the mid-wall and the inner most ring represents the apex. A standard 17 segment American Heart Association approved structure of the bull's eye was used (Figure 3-18). The bull'e eye plot was created in *Matlab*. The outermost and the middle ring were divided into 6 segments of 60˚ each with increasing angles in the counter clockwise direction. The innermost ring was divided into segments of 90˚ each with angles increasing in the counter clockwise direction.

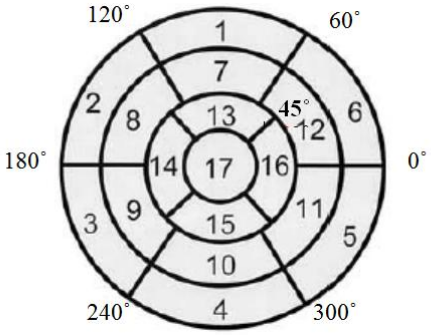

Figure 3-17: Diagram showing 17 segment circumferential polar plot and the recommended nomenclature for tomographic imaging of the heart [51].

Bull's eye plot representing the spatial distribution of the myocardial wall thickness generated from the 3D model has been shown below for each of the three models analyzed in this thesis. Figure 3-19 shows the bull's eye plot for patient 1, Figure 3-20 shows the bull's eye plots for patient 2.

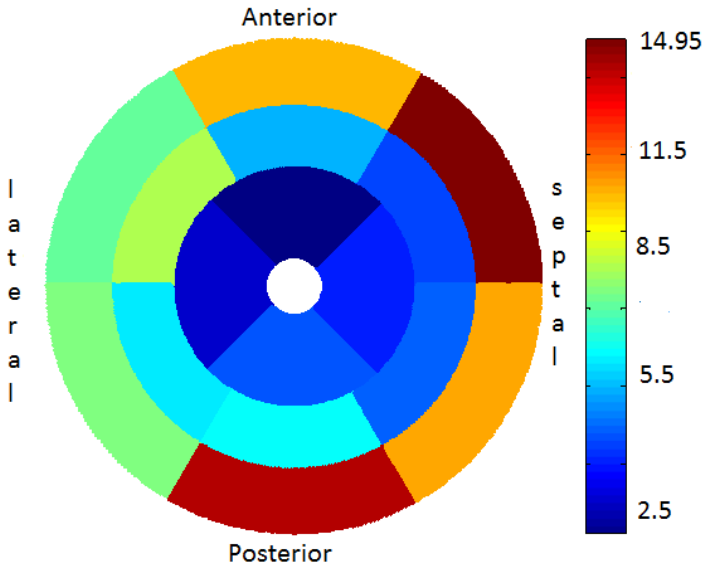

Figure 3-18: Bull's eye plot showing the spatial distribution of myocardial wall thickness in patient 2.

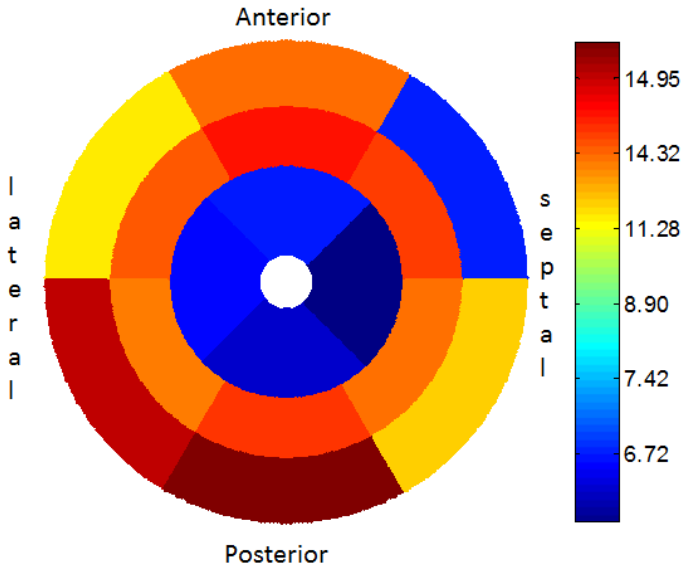

Figure 3-19: Bull's eye plot showing the spatial distribution of myocardial wall thickness in patient 2.

3.4 Ventricular Cavity and Wall Volume Estimation

Left ventricular and RVFW end-diastolic cavity volumes (LVEDV and RVFW-EDV) were calculated in *Continuity 6.3*. End-diastolic myocardial wall volume (MW-EDV) was calculated for all the three patient specific models. Left ventricular and right ventricular myocardial wall mass (LV Wall mass and RVFW mass) was calculated by multiplying wall volume by the wall density (1.05g/ml). The table 3-2 below shows the volume estimates for the two HF patients.

Table 3-2- Table showing the cavity and wall volume and mass

	Patient 1	**Patient 2**
LVEDV (ml)	211.5	330.9
RVFW-EDV (ml)	126.6	143.0
LV-MW-EDV (ml)	131.0	355.3
RV-MW-EDV (ml)	69.1	133.8
LV Wall mass (g)	137.5	373.1
RVFW mass (g)	72.5	140.5

To validate the results obtained from the 3D model, LV cavity volume was also calculated using cardiac images by applying the Simpson's method.

Table 3-3: Table comparing the LV cavity volume calculated using 3D model and Simpson's rule

	LVEDV (Model- ml)	**LVEDV(Simpson's method-**
Patient 1	211.5	205.6
Patient 2	330.9	338.2

4 Discussion

Patient-specific modeling has been proposed as a new paradigm in simulation based medical planning. Computational models can be used to construct and evaluate both anatomical and physiological models which can thereby predict the outcome of alternative treatment plans for a particular patient. Due to the extent of variability in structure and electromechanical properties in different patients, it is important to incorporate patient specific parameters into these computational models to accurately reproduce the behavior of the heart in response to a therapy. The goal of this thesis was to develop a methodology for building patient specific geometric models of the heart from clinical measurements such as cardiac CT and cardiac MRI which, in future, will be used to study the electromechanical behavior of the heart. These models can be tested for their predictive power of response to CRT by imposing ventricular pacing and computing global and local mechanical function. In addition, these multi-scale models

can be tested to predict acute reductions of ventricular end-systolic volumes during pacing in HF patients. In order to use patient specific models to predict the behavior of the heart in response to a condition, it is important to design efficient, quick and accurate methods to develop models from clinical measurements. In this thesis, an efficient method to develop three-dimensional biventricular model of the heart using cardiac images has been described. Techniques for image segmentation, initial finite element mesh generation and two-dimensional anatomic mesh fitting have been presented. Furthermore, three-dimensional patient specific models were used to estimate geometric parameters such as end-diastolic wall thicknesses and volumes. The results of the described methods for the development of patient-specific computational models to predict and optimize the outcomes of CRT are discussed in the following sections.

4.1 Image Segmentation

Cardiac CT and MR images are used for segmentation and model development. With the advent of 16-, and 64-slice CT scanners, improvements in temporal resolution and shortened acquisition time have led to the increasing usage of CT images as a useful imaging modality to develop 3D patient-specific models. Studies assessing both global and regional cardiac function analysis have shown cardiac CT to be a potential candidate for evaluating cardiac function [33, 34, 35]. Cardiac MR is widely accepted as the standard of reference for assessing cardiac function parameters. It is a noninvasive technique that provides excellent temporal resolution and soft-tissue contrast. Cardiac MR images typically have a slice thickness varying from 2-10mm

while CT images allows visualization of as less as 0.5mm in plane and a slice thickness of as low as 0.75mm. Although CT images offered high resolution, there were many artifacts present on the images which were noticed as sudden jumps in the series of images. These artifacts may occur as a result of irregular heart rhythm in patients with arrhythmia. ECG gating technique can be used to avoid these artifacts by correlating the CT data with their corresponding phases of cardiac contraction and separating data collected in motion or systole from the data collected during rest or diastole. Due to the presence of these artifacts, manual delineation of endocardial and epicardial surfaces had to be applied to those images that presented the artifacts.

Since both CT and MR images have an intensity contrast that is not very clear, image processing techniques such as contrast enhancement was used to improve the quality of the images. Since the epicardium exhibited a low contrast with chest cavity, compared to the contrast between endocardium and LV cavity, manual segmentation was used to extract the epicardial boundary.

The human heart contains blood vessels, papillary muscles and many trabeculae which were not modeled in this case. Hence, these structures were not included in the process of segmentation.

4.2 Model Development

A semi-automatic mesh generating method was described in this thesis using landmark points. It is an efficient and relatively less time-consuming method of making initial finite element meshes from cardiac images compared to the previously used method of connected nodes described later. This method uses prolate spheroidal

coordinates to build the mesh which is advantageous while performing 2D fitting. While prolate spheroidal coordinates requires fitting in only the radial coordinate (λ), rectangular cartesian coordinates requires fitting all three coordinates in the mesh (λ, μ, θ). An initial mesh built using this method closely resembles the geometry of the heart due to the use of anatomical markers as landmark points.

Before this method, an initial mesh in prolate spheroidal coordinate system was used, wherein the coordinate positions were arbitrarily chosen to place nodes at the anterior, posterior, lateral and mid-septal regions. Another, more interactive, method used to build initial meshes using the image editor in *Continuity 6.3* was the connected nodes method. This method allows the user to place nodes at the desired anatomical locations on the cardiac images. The connected nodes method essentially places a cylindrical tube on the stack of images where nodes at the same longitudinal level have to be placed on the same image slice. The disadvantage of using this method is that it assumes the images are short-axis. It also has limitations in performing transformations. The rotation function in this method allows just one rotation. In order to align the CT images along the long axis of the heart to match the model coordinate system, a series of rotations is required. The connected nodes method does not have the capability to add rotations and hence the data was improperly aligned. It can sometimes be readily used with MR images if they are short-axis slices but cannot be used with CT images. CT image slices are not short axis and requires the connected nodes at the same longitudinal level to be placed on different image slices. As a result, an initial mesh built from CT images using this method had tilted elements and required post-

processing in *Matlab* which included rotation of the nodes to align them circumferentially. This method is time consuming and not very efficient when used with cardiac CT images.

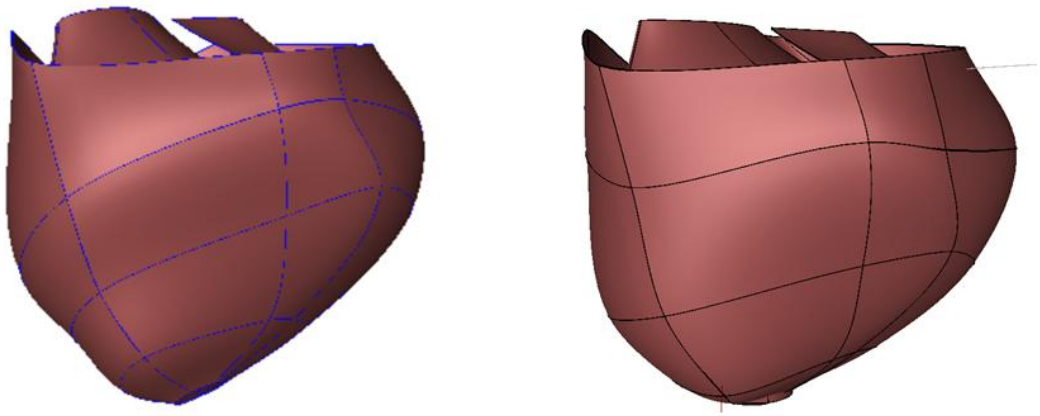

Figure 4-1: Posterior view of the initial mesh built using connected nodes (left) and after rotating nodes in Matlab (right).

In future, the landmark points method can be improved upon and further simplified by using fewer than seventeen landmark points to build an initial mesh and creating more nodes by interpolation between the landmark points. One of the possible ways is to reduce the number of landmark points to eight given by 5 basal points and 3 apical points- LV Lateral Basal Epicardium, RV Lateral Basal Endocardium, RV Anterior Basal Endocardium, RV Posterior Basal Endocardium, RV midseptal Basal Endocardium, RV Anterior Apical Endocardium, RV Posterior Apical Endocardium and LV Apical Epicardium.

4.3 Myocardial Wall Thickness Estimation

Global and regional left ventricular (LV) functions such as ejection fraction, wall motion, end-diastolic and end-systolic volumes are widely used indicators of cardiac disease [59]. LV ejection fraction and volume is often used to identify systolic and diastolic LV dysfunction, and to monitor the progression of the disease in patients with heart failure. Currently, many modalities are available to assess cardiac function like echocardiography, cineventriculography, cardiac CT and cardiac MR. These methods require subjective, visual estimation of global and regional ejection fraction in addition to being operator dependent [59]. In this thesis, patient specific cardiac geometric models were used to estimate the myocardial wall thickness. This method is reliable and efficient since the models closely resemble the actual geometry of the failing hearts obtained from segmenting cardiac images. The results obtained from the 3D model of the heart were compared to the values obtained from echocardiograms at the VAMC prior to BiV-ICD implant. The technique for analyzing ventricular function using 3D model and bull's eye plot can be user-dependent since the model is based on the accuracy of segmentation. Despite the possible variability in analysis, it is advantageous compared to echocardiography [37, 38, 39]. Images obtained from echocardiography are limited in quality and the accuracy of ventricular function determination is affected due to poor delineation of epicardium and endocardium.

Mean septal wall thickness of the two heart failure patients was calculated to 1.085 ± 0.22 cm (mean ± SD) and the LV free wall thickness was calculated to be 1.02 ± 0.34 cm (mean ± SD). Studies have shown that the normal human heart not in any

diseased state has a mean septal wall thickness of 1.38 ± 0.11 cm (mean ± SD) and a mean posterior wall thickness of 1.38 ± 0.07 cm (mean ± SD) [30]. Potential sources of error in data collection in this study compared to other studies and echocardiographically obtained thicknesses could be that the measurements were not made at precisely the same locations.

In the future, for finite element simulations, we need to calculate the unloaded cardiac geometries for these patients. The unloaded 3D geometrical model of the heart on performing further simulations would allow us to calculate the end-systolic wall thickness that would then facilitate the assessment of myocardial wall thickening in these heart failure patients. Therefore, 3D patient specific model of cardiac geometry can also be used to estimate the myocardial wall thickness. .

4.4 Ventricular Cavity and Wall Volume Estimation

Studies have demonstrated that the main predictor of responsiveness to CRT is mechanical rather than electrical dyssynchrony which makes the assessment of regional ventricular function very important [44, 45]. Ventricular end-diastolic volume is an important determinant of the global ventricular function such as cardiac output. Accurate estimation of dynamic LV volumes from patient specific models is very useful. End-diastolic and end-systolic LV volume measurements that are obtained from multiple cardiac cycles can be used to determine EDPVR and ESPVR which can then be used in the determination of passive and active mechanical parameters of the cardiac tissue. Moreover, P-V loops derived from the dynamic LV pressure and volume measurements is a useful means to evaluate global LV function and for validating the

model. In addition, stroke work defined as the area within the P-V loop could be useful refining the model at a later stage. Hence, it is important to develop efficient and reliable methods to examine the ventricular cavity and wall volumes. In this thesis, the 3D model patient specific models were used to calculate the end-diastolic volumes.

The LVEDV calculated for the patients in this study was 271.17 ± 84.34 ml (mean±SD). These volumes were comparable to those calculated using Simpson's method suggesting that using 3D models to calculate the volumes gives accurate results. It is important to note that these calculations involve a certain degree of error and are user-dependent due to manual tracings of the endocardial borders. This variability can be significantly reduced if the images used are high resolutions with a good contrast to enable precise identification of the endocardial and epicardial boundaries

5 Conclusion

Patient specific modeling has demonstrated great potential in its ability to improve diagnosis, optimize clinical treatment by predicting outcomes of therapies and surgical interventions. Since the existing diagnostic practices are based on the results of a few clinical trials, they are designed to cater to a large group of patients but may not necessarily be beneficial to all patients. On the other hand, use of patient specific models can be used as a theranostic tool to tailor treatment and optimize a patient's therapy. Due to this reason, patient specific modeling is gaining popularity among researchers worldwide. Significant efforts have been made by our group to validate these models in canine, mouse and rabbit models of arrhythmia and HF. It is now feasible to apply these modes in a clinical setting. However, no large clinical trials have been conducted to apply computational modeling strategies to clinical problems in patients. The overall goal of this research is to test the potential predictive ability of

these models to improve the outcomes of CRT in dyssynchronous HF patients by comparing to experimental results as well as explore the clinical feasibility of these models for physicians. For this purpose, patient specific models based on non-invasive medical imaging and in-vivo clinical measurements were developed in this thesis [50].

One of the reasons for patient specific modeling not being a standard of care in clinical settings is because these have not been researched on a large scale owing to the number of manual steps that goes into building and testing these models. In this thesis, a semi-automatic method for building a three-dimensional patient-specific finite element mesh requiring few manual steps was described. The process is efficient and comparatively less time-consuming. The proposed method generated an accurate 3D model of the failing human heart. However, this model does not include any trabeculae, papillary muscles, valves and the atria. A 3D model representing the cardiac geometry is an important step in computational modeling since a well-fit geometry is a key factor in determining global and regional ventricular function.

Myocardial wall thickness is an important parameter in determining regional ventricular function. The method proposed in this thesis to measure wall thickness used the 3D patient-specific model and the results were comparable to those obtained from echocardiograms thus validating the fit of the constructed geometric model.

Ventricular cavity volumes are also key parameters in assessing cardiac function. The proposed method calculates the volume from the 3D model that accurately resembles the ventricular geometry and is obtained from high resolution

modalities such as CT and MR. These volume calculations were also validated using the Simpson's method for volume estimation, thus validating the fit of the 3D model.

It is possible to develop accurate and efficient patient-specific computational models as a result of the methods described in this thesis. The highlight of this research is to develop a realistic geometric finite element model of the failing human heart. While a significant amount of research has been done on animal models, few attempts have been made to develop similar models for humans. To date, this is one of the first attempts to develop a computational patient specific model of a dyssynchronous human heart. Although these models may not provide a conclusive prediction of the requisite therapy, they certainly act as a reliable aid in studying cardiac geometry and function.

6 Appendices

6.1 Appendix A

Shown below are the seventeen landmark points identified on CT images for patient 2.

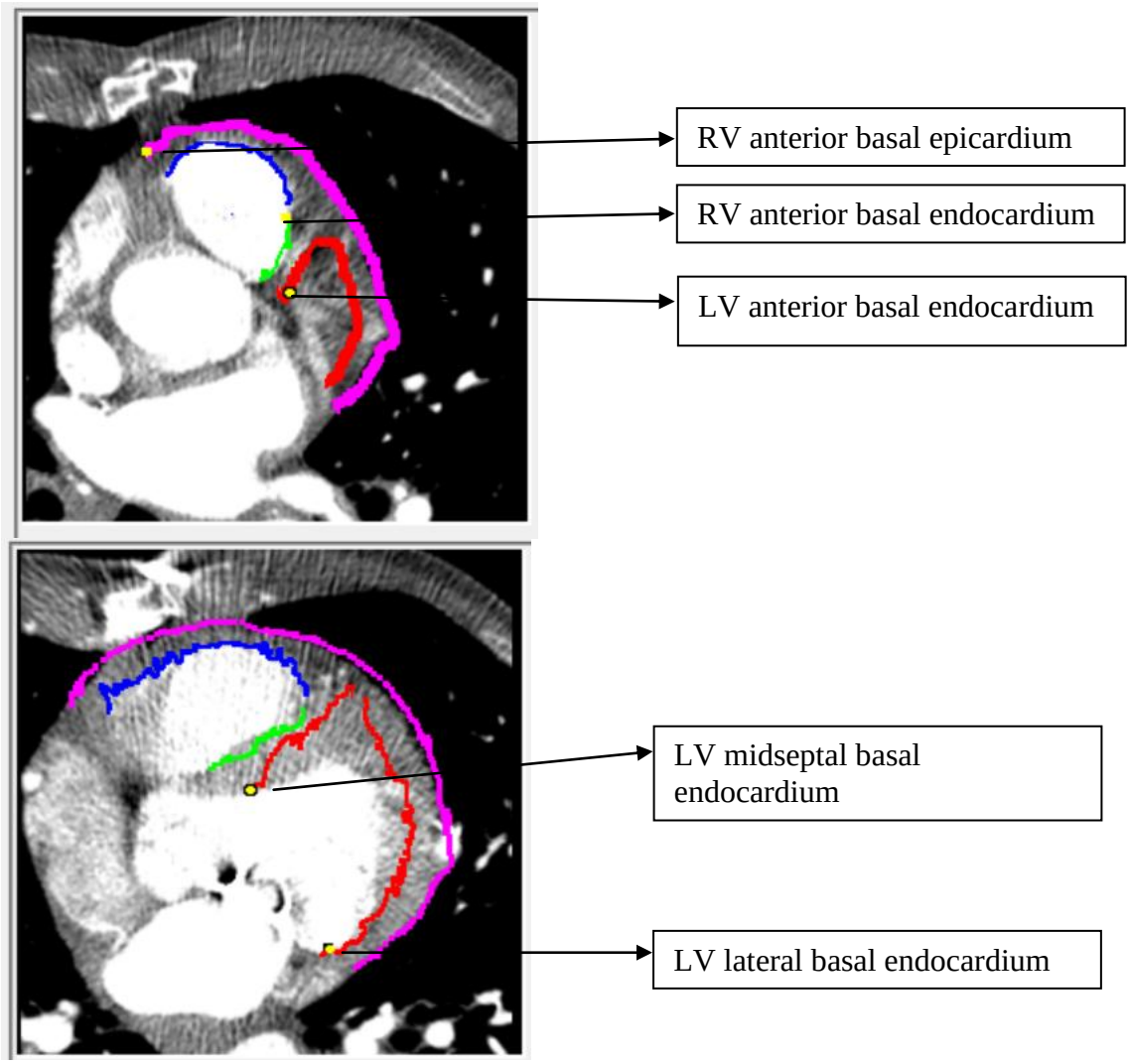

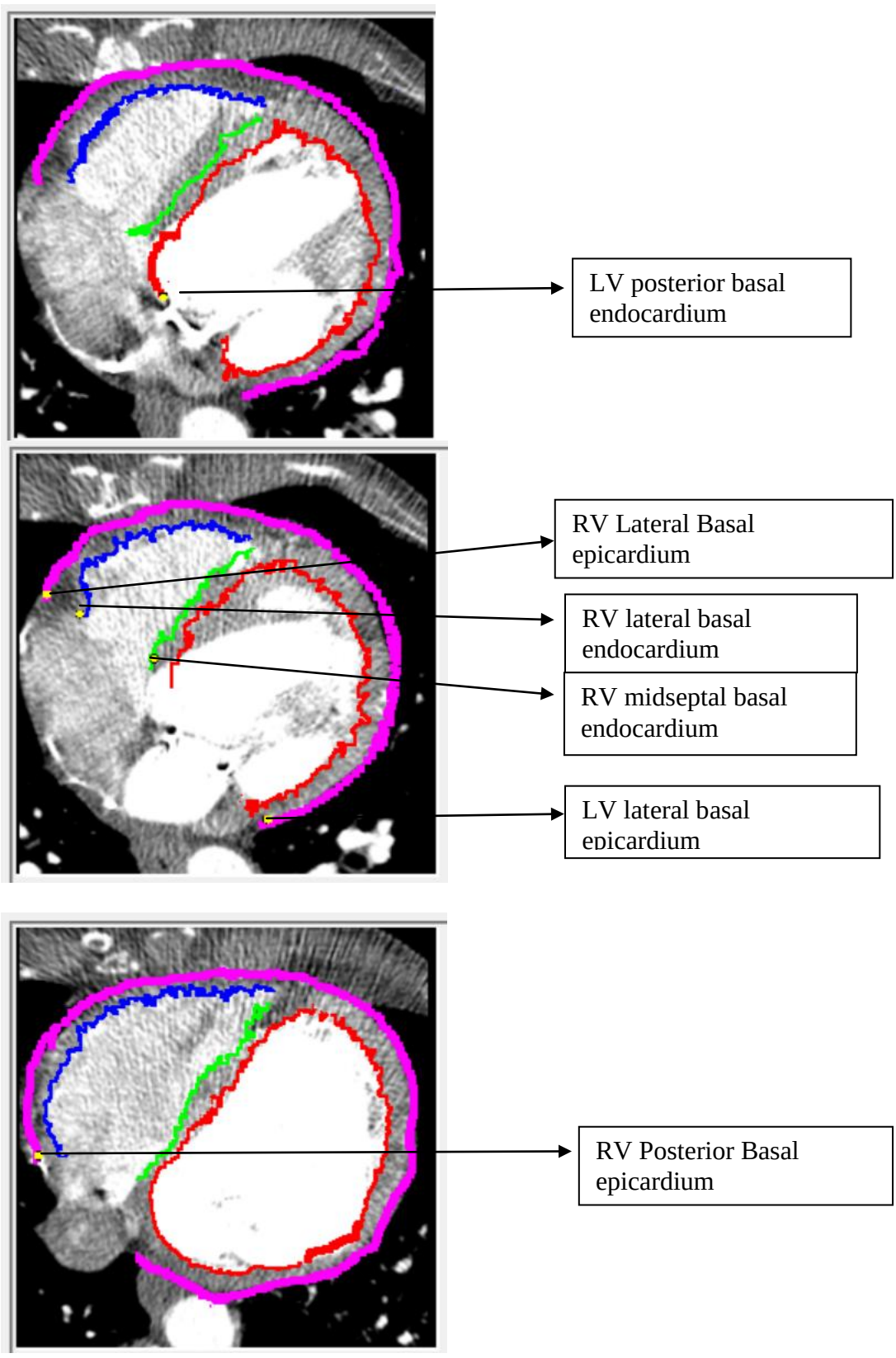
LV posterior basal endocardium
RV Lateral Basal epicardium
RV lateral basal endocardium
RV midseptal basal endocardium
LV lateral basal epicardium
RV Posterior Basal epicardium

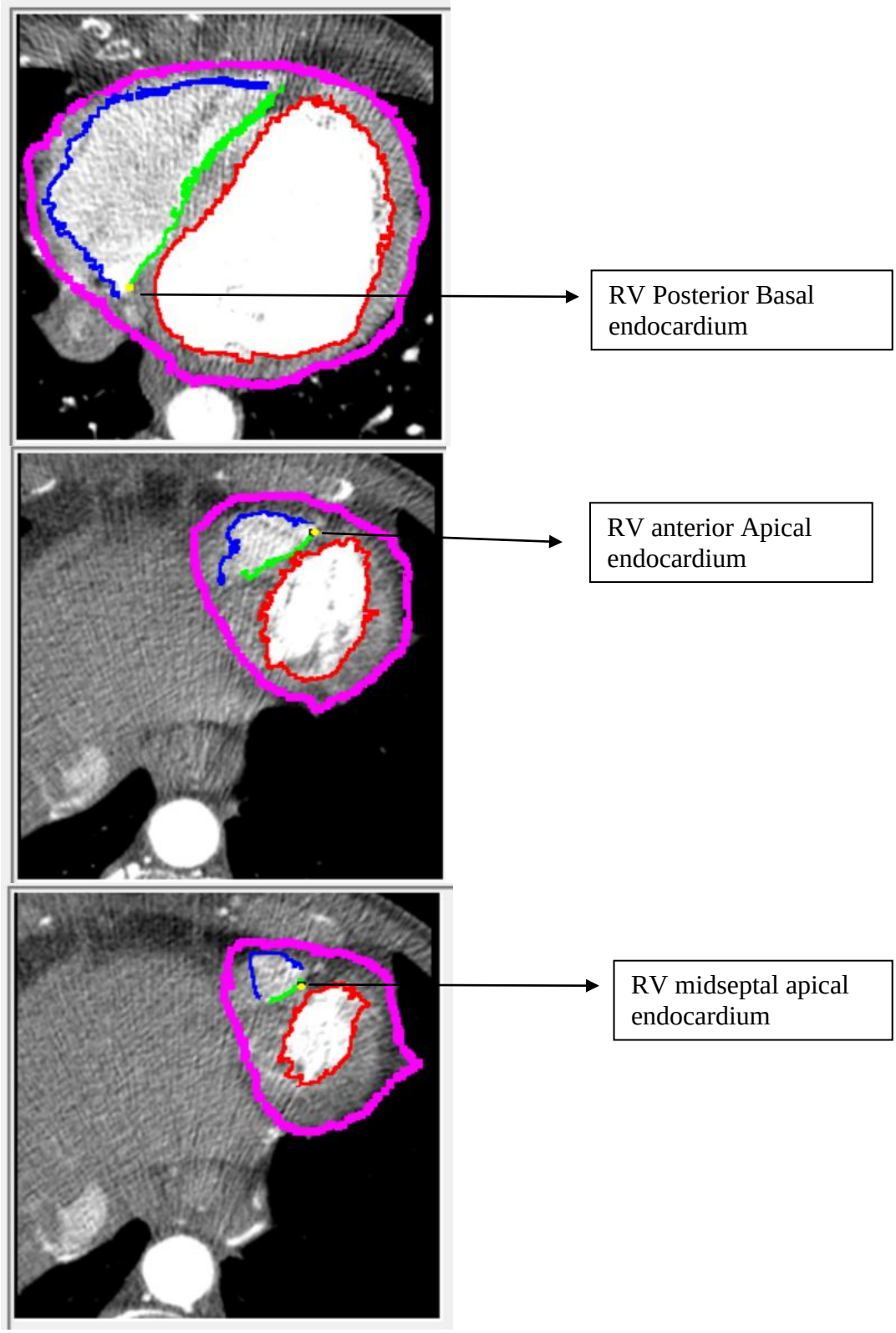
RV Posterior Basal endocardium
RV anterior Apical endocardium
RV midseptal apical endocardium

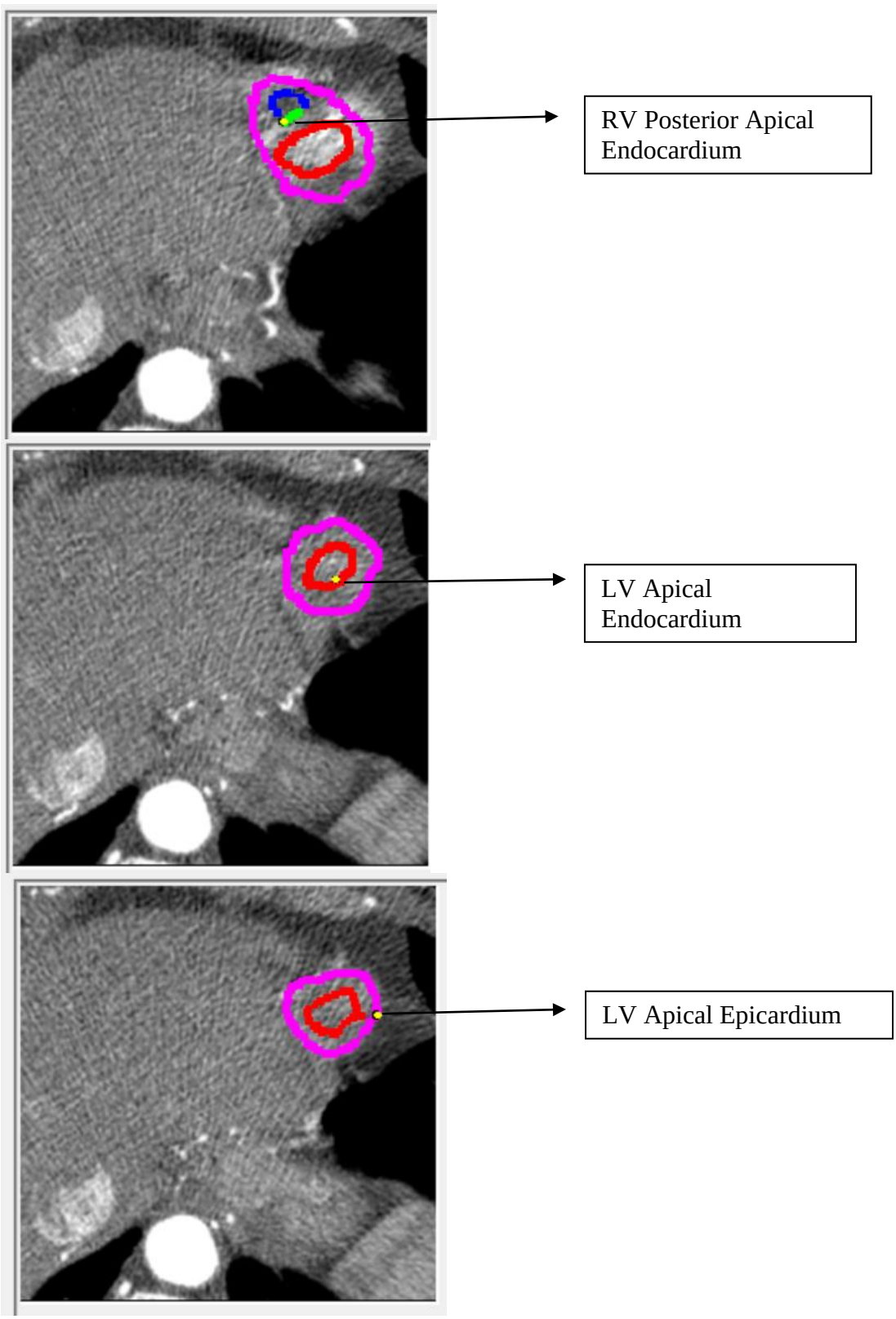
RV Posterior Apical Endocardium
LV Apical Endocardium
LV Apical Epicardium

6.2 Appendix B

M-file to convert rectangular cartesian coordinates to prolate spheroidal coordinates.

```
close all;
clear all;

x=[-6.602018292 -22.27667675    33.77448439
-28.70895642    -29.41910979    -8.959318271
-23.08525329    -33.64804313    9.319986624
-43.07499041    9.56135499  7.68737355
-10.78298855    -40.68263297    53.09706646
-21.42656372    -35.51878444    -24.26659537
-20.84036681    -38.81885933    9.145637409
-14.47852081    -66.40522866    6.00195744
-5.198606845    -44.24476542    57.17326558
-26.83645452    -40.64082275    -28.75097804
-8.465656681    -76.62325647    3.674644547
-37.37135785    22.06789182 3.382855262
60.47628858 -0.108660974    -1.651090225
51.21849069 -16.91895785    18.60131394
47.83967406 -17.86084072    0.147659849
66.86196616 1.747231997 -1.357770803
]; %nodes to be converted to prolate spheroidal coordinates

ca=x(13,1:3)-[0,0,0];
cm=x(3,1:3)-[0,0,0];
ca=sqrt(ca(1)^2+ca(2)^2+ca(3)^3);
cm=sqrt(cm(1)^2+cm(2)^2+cm(3)^3);
d1=sqrt(ca^2-cm^2); %calculate focal length from the major and minor
axis
prolate=zeros(length(x),3);
rect=zeros(length(x),3);
for i=1:length(x)
    x1=x(i,1);
    x2=x(i,2);
    x3=x(i,3);
    theta1=atan2(x3,x2);
    theta=theta1*180/pi; %calculates theta
        if theta<0          % 0<=theta<360
            theta=theta+360;
        end
    d=37; %use 37 for mm or the calculated d from Continuity
    c1=(x1^2/d^2)+((x2^2+x3^2)/d^2)+1; % defining the constants
(coefficients) of the quadratic from wiki
    c2=x1^2/d^2;
    n1=(c1+sqrt(c1^2-4*c2))/2; %n=cosh^2 lambda and n=cos^2 mu
    n2=(c1-sqrt(c1^2-4*c2))/2;
    n3=sqrt(n1);
    n4=sqrt(n2);
```

```
        if ((n3>1)|| (n3==0))&&n4<1 %n5 >1 to find inverse cosh and n6
<1 for find inverse cosine
            n5=n3;
            n6=n4;
        else
            n5=n4;
            n6=n3;
        end
    lambda=log((n5)+sqrt(n5^2-1)); %to get inverse cosh
    mu1=acosd(n6);
        if x1>0   %cos becomes negative for negative x1, setting this
condition gives correct mu which is in the second quadrant
            mu=mu1;
        else
            mu=180-mu1;
        end
    prolate(i,1:3)=[lambda, mu, theta];
    y1=d*cosh(lambda)*cosd (mu);
    y2=d*sinh(lambda)*sind(mu)*cosd(theta);
    y3=d*sinh(lambda)*sind(mu)*sind(theta);
    rect(i,1:3)=[y1, y2, y3];
end

xlswrite('prolate_data', prolate);
```

6.3 Appendix C

Python Script for node interpolation using 17 landmark points.

```
This will compute the remaining nodes that we need to define our mesh
from the original 17 landmarks that have already been converted into prolate
coordinates.
NOTE: This is obviously highly specific to the current task
(i.e., taking in 17 nodes (identified from specific landmarks) and computing a total of 50 nodes)
'''
def getCompleteNodeListFromLandmarks( self, worldProlatePoints ):
        # Create a new array to hold the new coords, as we need
        # a fair portion of the incoming list to be retained, just create
        # a copy and overwrite what we need
        # Define some index constants just to make it clear what's going on
        lambdaIndex = 0
        muIndex = 1
        thetaIndex = 2

        # These formulae rely on the fact that the worldProlatePoints are in the same order
        # landmarks as displayed on the GUI

        # Compute some values that are going to used for multiple nodes
        # lambdas
        lambdaEpi1 = worldProlatePoints[self.eif.landmarkNames.index('RV lateral basal
epicardium')][lambdaIndex]
        lambdaEpi2 = worldProlatePoints[self.eif.landmarkNames.index('RV posterior basal
epicardium')][lambdaIndex]
        lambdaEpi3 = worldProlatePoints[self.eif.landmarkNames.index('LV lateral basal
epicardium')][lambdaIndex]
        lambdaEpi4 = worldProlatePoints[self.eif.landmarkNames.index('RV anterior basal
epicardium')][lambdaIndex]
        lambdaST1 = worldProlatePoints[self.eif.landmarkNames.index('RV posterior basal
endocardium')][lambdaIndex]
        lambdaST2 = .5 * ( worldProlatePoints[self.eif.landmarkNames.index('LV lateral basal
epicardium')][lambdaIndex] +
                                                worldProlatePoints[self.eif.landmarkNames.index('LV
lateral basal endocardium*')][lambdaIndex] )
        lambdaST3 = worldProlatePoints[self.eif.landmarkNames.index('RV anterior basal
endocardium')][lambdaIndex]
        lambdaST4 = worldProlatePoints[self.eif.landmarkNames.index('RV midseptal basal
endocardium*')][lambdaIndex]
        lambdaST6 = worldProlatePoints[self.eif.landmarkNames.index('RV midseptal apical
endocardium*')][lambdaIndex]
        lambdaST7 = worldProlatePoints[self.eif.landmarkNames.index('RV posterior apical
endocardium')][lambdaIndex]
        lambdaST9 = worldProlatePoints[self.eif.landmarkNames.index('RV anterior apical
endocardium')][lambdaIndex]
        lambdaST5 = 0.5 *( lambdaST4 + lambdaST6 )
        lambdaRV1 = worldProlatePoints[self.eif.landmarkNames.index('RV posterior basal
endocardium')][lambdaIndex]
```

```
        lambdaEpi7 = worldProlatePoints[self.eif.landmarkNames.index('LV apical
epicardium')][lambdaIndex]
        lambdaLV1 = worldProlatePoints[self.eif.landmarkNames.index('LV midseptal basal
endocardium*')][lambdaIndex]
        lambdaLV2 = worldProlatePoints[self.eif.landmarkNames.index('LV posterior basal
endocardium')][lambdaIndex]
        lambdaLV3 = worldProlatePoints[self.eif.landmarkNames.index('LV lateral basal
endocardium*')][lambdaIndex]
        lambdaLV4 = worldProlatePoints[self.eif.landmarkNames.index('LV anterior basal
endocardium')][lambdaIndex]
        lambdaLV7 = worldProlatePoints[self.eif.landmarkNames.index('LV apical
endocardium*')][lambdaIndex]
        lambdaST10 = 0.5 * ( lambdaEpi7 + lambdaLV7 )
        lambdaratio = lambdaST6 / lambdaST10
        lambdaEpi6 = lambdaratio * lambdaEpi7
        lambdaLV6 = lambdaratio * lambdaLV7
        lambdaLV5 = 0.5 * (lambdaLV1+lambdaLV6)
        lambdaEpi5 = 0.5 * (lambdaEpi6+lambdaEpi1)
        # mus
        muEpi1 = worldProlatePoints[self.eif.landmarkNames.index('RV lateral basal
epicardium')][muIndex]
        muEpi2 = worldProlatePoints[self.eif.landmarkNames.index('RV posterior basal
epicardium')][muIndex]
        muEpi3 = worldProlatePoints[self.eif.landmarkNames.index('LV lateral basal
epicardium')][muIndex]
        muEpi4 = worldProlatePoints[self.eif.landmarkNames.index('RV anterior basal
epicardium')][muIndex]
        muST1 = worldProlatePoints[self.eif.landmarkNames.index('RV posterior basal
endocardium')][muIndex]
        muST2 = 0.5 * ( worldProlatePoints[self.eif.landmarkNames.index('LV lateral basal
epicardium')][muIndex] +
                                        worldProlatePoints[self.eif.landmarkNames.index('LV
lateral basal endocardium*')][muIndex] )

        muST4 = worldProlatePoints[self.eif.landmarkNames.index('RV midseptal basal
endocardium*')][muIndex]
        mu3ST = (( worldProlatePoints[self.eif.landmarkNames.index('RV midseptal apical
endocardium*')][muIndex] +
                   worldProlatePoints[self.eif.landmarkNames.index('RV posterior apical
endocardium')][muIndex] +
                   worldProlatePoints[self.eif.landmarkNames.index('RV anterior apical
endocardium')][muIndex] ) / 3.)
        muST3 = worldProlatePoints[self.eif.landmarkNames.index('RV anterior basal
endocardium')][muIndex]
        mu2ST = degrees( math.acos( radians(cos(muST4) + cos(mu3ST)) ))
        mu2Epi = degrees( math.acos( radians(cos(muEpi1) + cos(mu3ST)) ))
        muLV1 = worldProlatePoints[self.eif.landmarkNames.index('LV midseptal basal
endocardium*')][muIndex]
        muLV2 = worldProlatePoints[self.eif.landmarkNames.index('LV posterior basal
endocardium')][muIndex]
        muLV3 = worldProlatePoints[self.eif.landmarkNames.index('LV lateral basal
endocardium*')][muIndex]
```

```
        muLV4 = worldProlatePoints[self.eif.landmarkNames.index('LV anterior basal
endocardium')][muIndex]
        mu2LV = degrees( math.acos( radians(cos(muLV1) + cos(mu3ST)) ))
        mu3LV = mu3ST
        muRVFW = worldProlatePoints[self.eif.landmarkNames.index('RV posterior basal
epicardium')][muIndex]
        # thetas
        thetaEpi1 = worldProlatePoints[self.eif.landmarkNames.index('RV lateral basal
epicardium')][thetaIndex]
        thetaEpi2 = worldProlatePoints[self.eif.landmarkNames.index('RV posterior basal
epicardium')][thetaIndex]
        thetaEpi3 = worldProlatePoints[self.eif.landmarkNames.index('LV lateral basal
epicardium')][thetaIndex]
        thetaEpi4 = worldProlatePoints[self.eif.landmarkNames.index('RV anterior basal
epicardium')][thetaIndex]
        thetaEpiApex2 = worldProlatePoints[self.eif.landmarkNames.index('RV midseptal apical
endocardium*')][thetaIndex]
        thetaEpiApex1= thetaEpi1
        thetaST1 = worldProlatePoints[self.eif.landmarkNames.index('RV posterior basal
endocardium')][thetaIndex]
        thetaST2 = 0.5 * ( worldProlatePoints[self.eif.landmarkNames.index('LV lateral basal
epicardium')][thetaIndex] +
                                        worldProlatePoints[self.eif.landmarkNames.index('LV
lateral basal endocardium*')][thetaIndex] )
        thetaST3 = worldProlatePoints[self.eif.landmarkNames.index('RV anterior basal
endocardium')][thetaIndex]
        thetaST4 = worldProlatePoints[self.eif.landmarkNames.index('RV midseptal basal
endocardium*')][thetaIndex]
        thetaST5 = worldProlatePoints[self.eif.landmarkNames.index('RV midseptal apical
endocardium*')][thetaIndex]
        thetaST6 = worldProlatePoints[self.eif.landmarkNames.index('RV posterior apical
endocardium')][thetaIndex]
        thetaST7 = worldProlatePoints[self.eif.landmarkNames.index('RV anterior apical
endocardium')][thetaIndex]
        thetaLV1 = worldProlatePoints[self.eif.landmarkNames.index('LV midseptal basal
endocardium*')][thetaIndex]
        thetaLV2 = worldProlatePoints[self.eif.landmarkNames.index('LV posterior basal
endocardium')][thetaIndex]
        thetaLV3 = worldProlatePoints[self.eif.landmarkNames.index('LV lateral basal
endocardium*')][thetaIndex]
        thetaLV4 = worldProlatePoints[self.eif.landmarkNames.index('LV anterior basal
endocardium')][thetaIndex]
        theta3ST = 0.5 * ( thetaLV3 + thetaEpi3 )
        thetaRVFW1 = worldProlatePoints[self.eif.landmarkNames.index('RV posterior basal
epicardium')][thetaIndex]
        thetaEpiApex2=thetaEpiApex1+90
        if thetaEpiApex2 > 360:
                thetaEpiApex2 = thetaEpiApex2 - 360
        thetaEpiApex3 = thetaEpiApex1 + 180
        if thetaEpiApex3 > 360:
                thetaEpiApex3 = thetaEpiApex3 - 360
        thetaEpiApex4 = thetaEpiApex1 + 270
        if thetaEpiApex4 > 360:
```

```
        thetaEpiApex4 = thetaEpiApex4 - 360


# Assemble the nodes
# Node 1
nodeList = []
nodeList.append( [ lambdaEpi1,
                                    muEpi1,
                                    thetaST4,
                                    'Epi', 1.0, 1.0, 1.0, 1.0 ] )
# Node 2
nodeList.append( [ lambdaEpi2,
                                    muEpi2,
                                    thetaST1,
                                    'Epi', 1.0, 1.0, 1.0, 1.0 ] )
# Node 3
nodeList.append( [ lambdaEpi3,
                                    muEpi3,
                                    thetaEpi3,
                                    'Epi', 1.0, 1.0, 1.0, 1.0 ] )
# Node 4
nodeList.append( [ lambdaEpi4,
                                    muEpi4,
                                    thetaST3,
                                    'Epi', 1.0, 1.0, 1.0, 1.0 ] )
# Node 5
nodeList.append( [ lambdaEpi5,
                                    mu2ST,
                                    thetaST4,
                                    'Epi', 1.0, 1.0, 1.0, 1.0 ] )
# Node 6
nodeList.append( [ lambdaEpi5,
                                    mu2ST,
                                    thetaST1,
                                    'Epi', 1.0, 1.0, 1.0, 1.0 ] )
# Node 7
nodeList.append( [ lambdaEpi5,
                                    mu2ST,
                                    thetaEpi3,
                                    'Epi', 1.0, 1.0, 1.0, 1.0 ] )
# Node 8
nodeList.append( [ lambdaEpi5,
                                    mu2ST,
                                    thetaST3,
                                    'Epi', 1.0, 1.0, 1.0, 1.0 ] )
# Node 9
nodeList.append( [ lambdaEpi6,
                                    mu3ST,
                                    thetaST4,
                                    'Epi', 1.0, 1.0, 1.0, 1.0 ] )
# Node 10
nodeList.append( [ lambdaEpi6,
                                    mu3ST,
```

```
                                        thetaST1,
                                        'Epi', 1.0, 1.0, 1.0, 1.0 ] )
# Node 11
nodeList.append( [ lambdaEpi6,
                                        mu3ST,
                                        thetaEpi3,
                                        'Epi', 1.0, 1.0, 1.0, 1.0 ] )
# Node 12
nodeList.append( [ lambdaEpi6,
                                        mu3ST,
                                        thetaST3,
                                        'Epi', 1.0, 1.0, 1.0, 1.0 ] )
# Node 13
nodeList.append( [ lambdaEpi7,
                                        0.0,
                                        thetaEpiApex1,
                                        'Epi', 1.0, 1.0, 1.0, 1.0 ] )
# Node 14
nodeList.append( [ lambdaRV1,
                                        muRVFW,
                                        thetaST4,
                                        'RVFW', 1.0, 1.0, 1.0, 1.0 ] )
# Node 15
nodeList.append( [ lambdaST1,
                                        muST1,
                                        thetaST1,
                                        'ST', 1.0, 1.0, 1.0, 1.0 ] )
# Node 16
nodeList.append( [ lambdaST2,
                                        muST2,
                                        thetaEpi3,
                                        'ST', 1.0, 1.0, 1.0, 1.0 ] )
# Node 17
nodeList.append( [ lambdaST3,
                                        muST3,
                                        thetaST3,
                                        'ST', 1.0, 1.0, 1.0, 1.0 ] )
# Node 18
nodeList.append( [ lambdaST4,
                                        muST4,
                                        thetaST4,
                                        'ST', 1.0, 1.0, 1.0, 1.0 ] )
# Node 19
nodeList.append( [ 0.5 * (lambdaRV1 + lambdaST6),
                                        mu2ST,
                                        thetaST4,
                                        'RVFW', 1.0, 1.0, 1.0, 1.0 ] )
# Node 20
nodeList.append( [ lambdaST5,
                                        mu2ST,
                                        thetaST1,
                                        'ST', 1.0, 1.0, 1.0, 1.0 ] )
```

```
# Node 21
nodeList.append( [ lambdaST5,
                   mu2ST,
                   thetaEpi3,
                   'ST', 1.0, 1.0, 1.0, 1.0 ] )
# Node 22
nodeList.append( [ lambdaST5,
                   mu2ST,
                   thetaST3,
                   'ST', 1.0, 1.0, 1.0, 1.0 ] )
# Node 23
nodeList.append( [ lambdaST5,
                   mu2ST,
                   thetaST4,
                   'ST', 1.0, 1.0, 1.0, 1.0 ] )
# Node 24
nodeList.append( [ lambdaST9,
                   mu3ST,
                   thetaST4,
                   'ST', 1.0, 1.0, 1.0, 1.0 ] )
# Node 25
nodeList.append( [ lambdaST6,
                   mu3ST,
                   thetaST1,
                   'ST', 1.0, 1.0, 1.0, 1.0 ] )
# Node 26
nodeList.append( [ lambdaST7,
                   mu3ST,
                   thetaEpi3,
                   'ST', 1.0, 1.0, 1.0, 1.0 ] )
# Node 27
nodeList.append( [ lambdaST6,
                   mu3ST,
                   thetaST3,
                   'ST', 1.0, 1.0, 1.0, 1.0 ] )
# Node 28
nodeList.append( [ lambdaST10,
                   0.0,
                   thetaEpiApex1,
                   'ST', 1.0, 1.0, 1.0, 1.0 ] )
# Node 29
nodeList.append( [ lambdaLV1,
                   muLV1,
                   thetaST4,
                   'LV', 1.0, 1.0, 1.0, 1.0 ] )
# Node 30
nodeList.append( [ lambdaLV2,
                   muLV2,
                   thetaST1,
                   'LV', 1.0, 1.0, 1.0, 1.0 ] )
# Node 31
nodeList.append( [ lambdaLV3,
                   muLV3,
```

```
                                    thetaEpi3,
                                    'LV', 1.0, 1.0, 1.0, 1.0 ] )
# Node 32
nodeList.append( [ lambdaLV4,
                                    muLV4,
                                    thetaST3,
                                    'LV', 1.0, 1.0, 1.0, 1.0 ] )
# Node 33
nodeList.append( [ lambdaLV5,
                                    mu2LV,
                                    thetaST4,
                                    'LV', 1.0, 1.0, 1.0, 1.0 ] )
# Node 34
nodeList.append( [ lambdaLV5,
                                    mu2LV,
                                    thetaST1,
                                    'LV', 1.0, 1.0, 1.0, 1.0 ] )
# Node 35
nodeList.append( [ lambdaLV5,
                                    mu2LV,
                                    thetaEpi3,
                                    'LV', 1.0, 1.0, 1.0, 1.0 ] )
# Node 36
nodeList.append( [ lambdaLV5,
                                    mu2LV,
                                    thetaST3,
                                    'LV', 1.0, 1.0, 1.0, 1.0 ] )
# Node 37
nodeList.append( [ lambdaLV6,
                                    mu3LV,
                                    thetaST4,
                                    'LV', 1.0, 1.0, 1.0, 1.0 ] )
# Node 38
nodeList.append( [ lambdaLV6,
                                    mu3LV,
                                    thetaST1,
                                    'LV', 1.0, 1.0, 1.0, 1.0 ] )
# Node 39
nodeList.append( [ lambdaLV6,
                                    mu3LV,
                                    thetaEpi3,
                                    'LV', 1.0, 1.0, 1.0, 1.0 ] )
# Node 40
nodeList.append( [ lambdaLV6,
                                    mu3LV,
                                    thetaST3,
                                    'LV', 1.0, 1.0, 1.0, 1.0 ] )
# Node 41
nodeList.append( [ lambdaLV7,
                                    0.0,
                                    thetaEpiApex1,
                                    'LV', 1.0, 1.0, 1.0, 1.0 ] )
# Node 42
```

```
nodeList.append( [ lambdaEpi7,
                                        0.0,
                                        (thetaEpiApex2),
                                        'EPI', 1.0, 1.0, 1.0, 1.0 ] )
# Node 43
nodeList.append( [ lambdaEpi7,
                                        0.0,
                                        (thetaEpiApex3),
                                        'EPI', 1.0, 1.0, 1.0, 1.0 ] )
# Node 44
nodeList.append( [ lambdaEpi7,
                                        0.0,
                                        (thetaEpiApex4),
                                        'EPI', 1.0, 1.0, 1.0, 1.0 ] )
# Node 45
nodeList.append( [ lambdaST10,
                                        0.0,
                                        (thetaEpiApex2),
                                        'ST', 1.0, 1.0, 1.0, 1.0 ] )
# Node 46
nodeList.append( [ lambdaST10,
                                        0.0,
                                        (thetaEpiApex3),
                                        'ST', 1.0, 1.0, 1.0, 1.0 ] )
# Node 47
nodeList.append( [ lambdaST10,
                                        0.0,
                                        (thetaEpiApex4),
                                        'ST', 1.0, 1.0, 1.0, 1.0 ] )
# Node 48
nodeList.append( [ lambdaLV7,
                                        0.0,
                                        (thetaEpiApex2),
                                        'LV', 1.0, 1.0, 1.0, 1.0 ] )
# Node 49
nodeList.append( [ lambdaLV7,
                                        0.0,
                                        (thetaEpiApex3),
                                        'LV', 1.0, 1.0, 1.0, 1.0 ] )
# Node 50
nodeList.append( [ lambdaLV7,
                                        0.0,
                                        (thetaEpiApex4),
                                        'LV', 1.0, 1.0, 1.0, 1.0 ] )

return nodeList
```

References

1) Katz AM. Physiology of the heart. Philadelphia, PA: Lippincott Williams & Wilkins, 2001.

2) Alters & Alters, *Biology:* Understanding Life, First Edition, *John Wiley & Sons, Inc.* © 2006 and Sumanas, Inc.

3) McCulloch AD (2005) Cardiac Biomechanics. Chapter 54 in: *The Biomedical Engineering Handbook*, 3rd Edition, Volume I, Bronzino JD, Editor-in-Chief, CRC Press, Boca Raton, FL: pages 54-1 to 54-27.

4) Vetter FJ, McCulloch AD (1998). Three-dimensional analysis of regional cardiac anatomy. *Progress in Biophysics and Molecular Biology* 69:157-183.

5) Streeter, D.D., Jr. and Hanna, W.T., Engineering mechanics for successive states in canine left ventricular myocardium: I. Cavity and wall geometry, *Circ. Res.*, 33, 639–655, 1973.

6) Nielsen, P.M.F., Le Grice, I.J., Smaill, B.H., Mathematical model of geometry and fibrous structure of the heart, *Am. J. Physiol.*, 260, H1365–H1378, 1991.

7) Young, A.A. and Axel, L., Three-dimensional motion and deformation in the heart wall: estimation from spatial modulation of magnetization — a model-based approach, *Radiology*, 185, 241–247, 1992.

8) *American Heart Association*, Heart disease and stroke statistics-2005 update. http://www.americanheart.org/presenter.jhtml?identifier=3000090. Accessed June 6, 2005.

9) Hofman A (2009). "The Rotterdam Study: 2010 objectives and design update". *Eur. J. Epidemiol* 24(9): 553-572. doi:10.1007/s10654-009-9386-z.

10) www.americanheart.org.

11) O'Connell JB, Bristow MR, Economic impact of heart failure in the United States: time for a different approach. J Heart Lung Transplant 1993; 13:S107-S112.

12) Parmley WW. Cost-effective cardiology: cost-effective management of heart failure. *Clin Cardiol* 1996; 19-240-242

13) The Criteria Committee of the New York Heart Association. Nomenclature and Criteria for Diagnosis of Diseases of the Heart and Great Vessels. *9th ed. Boston, Mass: Little, Brown & Co*; 1994:253-256.

14) http://en.wikipedia.org/wiki/New_York_Heart_Association_Functional_Classification.

15) McMurray JJ, Pfeffer MA. Heart failure. *Lancet* 365:1877–89, 2005.

16) Bleumink GS, Knetsch AM, Sturkenboom MCJM, Straus SMJM, Hofman A, Deckers JW, Witteman JCM, and Stricker BHC. Quantifying the heart failure epidemic: prevalence, incidence rate, lifetime risk and prognosis of heart failure: The Rotterdam Study 1614-1619, 2004.

17) Reis, SE, Holubkov, R, Edmundowicz, D, Treatment of patients admitted to the hospital with congestive heart failure: specialty-related disparities in practice patterns and outcomes. *J Am Coll Cardiol* 1997; 30:733.

18) Cardiac Resynchronization Therapy, DAVID A. KASS, M.D. From the Johns Hopkins Medical Institutions, Baltimore, Maryland, USA.

19) Baker J., Mckenzie J., Beau S., Greer GS, Porterfield J., Fedor M., Greenberg S, Daoud E., Corbisiero R, Bailey R, Porterfield L, Acute Evaluation of programmer-guided AV/PV and VV Delay optimization comparing an IEGM method and echocardiogram for cardiac resynchronization therapy in heart failure patients and dual-chamber ICD implants. *J Cardiovasc Electrophysiol*. 18:185-191, 2007.

20) http://en.wikipedia.org/wiki/Rotation_matrix

21) Mazhari R, Omens JH, Waldman LK, McCulloch AD. Regional myocardial perfusion mechanics: a model-based method of analysis. *Ann Biomed Eng* 26:743-755, 1998.

22) Woods RH: A few applications of a physical theorem to membranes in the human body in a state of tension. *J Anat Physiol* 26:362-370, 1892.

23) Burton AC: The importance of the shape and size of the heart. *Am Heart J* 54:801-810, 1957.

24) Maxwell Lewis Neal, Kerckhoffs Roy, Current Progress in patient-specific modeling. *Briefings in Bioinformatics* 11, 111-26.

25) Donald L. King, MD, Lyna El-Khoury Coffin, BS, RDCS, and Mathew S. Maurer, MD, Noncompressibility of Myocardium During Systole with Freehand Three-Dimensional Echocardiography. *American Journal of Echocardiography* 2002 doi:10.1067/mje.2002.126418.

26) Kerckhoffs RCP, McCulloch AD, Omens JH, Mulligan LJ (2008) Effects of biventricular pacing and scar size in a computational model of the failing heart with left bundle branch block. (2009) *Medical Image Analysis* 13: 362-369.

27) Troy B.L, Pombo J, Rackley C.E, Measurement of Left Ventricular Wall Thickness and mass by Echocardiography, *Circulation* 1972;45;602-611.

28) Kerckhoffs RCP, Lumens J, Vernooy K, Omens JH, Mulligan LJ, Delhaas T, Arts T, McCulloch AD, Prinzen FW (2008) Cardiac Resynchronization: insight from experimental and computational models. *Progress in Biophysics and Molecular Biology* Jun-Jul 2008;97:543-561. Doi:10.1016/j.pbiomolbio. 2008.02.024.

29) Carolyn S.P. Lam, M.R.C.P., Jasmine Grewal, Barry A. Borlaug, Steve R. Ommen, Garvan C. Kane, Robert B. McCully, and Patricia A. Pellikka, Size, Shape and Stamina: The Impact of Left Ventricular Geometry on Exercise Capacity, *Hypertension*. 2010 May; 55(5):1143 1149. doi:10.1161/HYPERTENSIONAHA.109.146845.

30) Sasayama S, Franklin D, Ross J. Jr, Kemper W.S, McKnown D, Dynamic Changes in Left Ventricular Wall Thicknesses and Their Use in Analyzing Cardiac Function in the Conscious Dog. *American Journal of Cardiology, Dec 1976. Vol 38.*

31) S.A. Hayat, G. Dwivedi, A. Jacobsen, T.K. Lim, C. Kinsey, R. Senior,. Effects of Left Bundle-Branch Block on Cardiac Structure, Function, Perfusion, and Perfusion Reserve Implications for Myocardial Contrast Echocardiography Versus Radionuclide Perfusion Imaging for the Detection of Coronary Artery Disease *Circulation* 2008;117;1832-1841.

32) E. Heiberg, L. Wigström, M. Carlsson, A. F. Bolger, and M. Karlsson, Time Resolved Three-dimensional Automated Segmentation of the Left Ventricle. In *Proceedings of IEEE Computers in Cardiology* 2005(32), pp. 599-602, Lyon, France, 2005.

33) Busch S, Johnson TR, Wintersperger BJ, Minaifar N, Bhargava A, Rist C, Reiser MF, Becker C, Nikolaou K, Quantitative assessment of left ventricular function with dual-source CT in comparison to cardiac magnetic resonance imaging: initial findings. *Eur Radiol*. 2008;18:570 –575.

34) Wu YW, Tadamura E, Yamamuro M, Kanao S, Okayama S, Ozasa N, Toma M, Kimura T, Komeda M, Togashi K, Estimation of global and regional cardiac function using 64-slice computed tomography: a comparison study with echocardiography, gated-SPECT and cardiovascular magnetic resonance. *Int J Cardiol*. 2008;128:69 –76.

35) Zhang Y., Bazilevs Y., Goswami S., Bajaj C.L., Hughes, T J.R., Patient-Specific Vascular NURBS Modeling for Isogeometric Analysis of Blood Flow. *Comput Methods Appl Mech Eng* 2007; 196 (29-30); 2943-2959.

36) Hoffman R, von Bardeleben S, Kasprzak JD, Borges AC, Cate FT, Firchke C, Lafitte S, Al-Saadi N, Kuntz-Hehner S, Horstick G, Greis C, Engelhardt M, Vanoverschelde JL, Becher H, Analysis of regional left ventricular function by cineventriculography, cardiac magnetic resonance imaging, and unenhanced and contrast-enhanced echocardiography – a multicenter comparison of methods. *J Am Coll Cardiol*. 2006;47:121–128.

37) Bellenger NG, Burgess MI, Ray SG, Lahiri A, Coats AJ, Cleland JG, Pennel DJ, Comparison of left ventricular ejection fraction and volumes in heart failure by echocardiography, radionuclide ventriculography and cardiovascular magnetic resonance; are they interchangeable? *Eur Heart J*. 2000;21:1387–1396.

38) Earls JP, Ho VB, Foo TK, Castillo E, Flamm SD, Cardiac MRI: recent progress and continued challenges. *J Magn Reson Imaging*. 2002;16:111–127.

39) Kaul S., Wismer G.L, Brady T.J., Johnston D.L., Weyman A.E., Okada R.D., Dinsmore R.E., Measurement of normal left heart dimension using optimally oriented MR images, *AJR 146:75*, January 1986 0361-803X/86/1461-0075.

40) Segers P, Rietzschel ER, De Buyzere ML, Vermeersch SJ, De Bacquer D, Van Bortel LM, De Backer G, Gillebert TC, Verdonck PR. Noninvasive (input) impedance, pulse, wave velocity, and wave reflection in healthy middle-aged men and women. *Hypertension.* 2007;49(6):1248-1255.

41) Rietzschel ER, De Buyzere ML, Bekaert S, Segers P, De Bacquer D, Cooman L, Van Damme P, Cassiman P, Langlois M, van Oostveldt P, Verdonck P, De Backer G, Gillebert TC. Rationale, design, methods and baseline characteristics of the Asklepios Study. *Eur J Cardiovasc Prev Rehabil.* 2007;14(2):179-191.

42) Nichols WW and O'Rourke MF. McDonald's blood flow in arteries. Theoretical, Experimental and Clinical Principles. 5 ed: *Oxford University Press*; 2005.

43) Pitzalis MV, Iacoviello M, Romito R, Massari F, Rizzon B, Luzzi G, Guida P, Andriana A, Mastropasqua F, Rizzon P, Cardiac resynchronization therapy tailored by echocardiographic evaluation of ventricular asynchrony. *J Am Coll Cardiol* 2002;40:1615–22.

44) Pitzalis MV, Iacoviello M, Romito R, Guida P, De Tommasi E, Luzzi G, Anaclerio M, Forleo C, Rizzon P, Ventricular asynchrony predicts a better outcome in patients with chronic heart failure receiving cardiac resynchronization therapy. *J Am Coll Cardiol* 2005;45:65–9.

45) Lim P., Bars C., Mitchell-Heggs L., Roiron C., Elbaz N., Hamdaoui B., Lellouche N., Dubois-Rande´ L., Gue´ret P., Importance of contractile reserve for CRT, *Europace* (2007) 9, 739–743 doi:10.1093/europace/eum117.

46) Grothues F., Smith G.C, Moon J.C.C, Bellenger N., Collins P., Klein H.U, Pennell D.J, Comparison of Interstudy Reproducibility of Cardiovascular Magnetic Resonance With Two-Dimensional Echocardiography in Normal Subjects and in Patients With Heart Failure or Left Ventricular Hypertrophy, *The American Journal of Cardiology*, Vol 90 July 1, 2002.

47) McCulloch, AD. "Multi-Scale Modeling Environment for Tissue and Organ Biophysics." Department of Bioengineering, University of California, San Diego, 30 Oct. 2008.

48) Hunter, P.J., McCulloch, A.D, Nielson, P.M.F., Smaill, B.H., 1988. A finite element model of passive ventricular mechanics. In: Spiker, R.L., Simon, B.R. (Eds.), Computational Methods in Bioengineering, vol 9. *American Society of Mechanical Engineers*, New York, NY pp. 387-397.

49) Cerqueira M.D., Weissman N.J, Dilsizian V., Jacobs A.K, Kaul S., Laskey W.K, Pennell D.J., Rumberger J.A., Ryan T., Verani M.S., "Standardized myocardial segmentation and nomenclature for tomographic imaging of the heart*", J Nucl Cardiol* 2002;9:240-5.

50) Neal M, Kerchoffs RCP(2010) Current Progress in Patient-Specific Modeling. *Briefings in Bioinformatics* 11, 111-26.

51) Le Grice I.J., Hunter P.J., Young A., Smaill B., The architecture of the heart: a data-based model, *Phil. Trans. R. Soc. Lond. A (2001)* 359, 1217-1232.

52) Costa KD, Hunter PJ, Rogers JM, Wayne JS, Guccione JM, Waldman LK, McCulloch AD (1996a,b), A three-dimesnional finite element method for large elastic deformations of ventricular myocardium: Part I- Cylindrical and spherical polar coordinates and Part II- Prolate spheroidal coordinates. *Journal of Biomechanical Engineering* 118: 452-472.

53) Bishop MJ, Plank G, Burton R, Schneider JE, Gavaghan DJ, Grau V, Kohl P, Development of an anatomically detailed MRI-derived rabbit ventricular model and assessment of its implact on simulations of electrophysiological function. *Am J Physiol Heart Circ Physiol* 298: H699-H718, 2010.

54) Vadakkumpadan F, Arevalo H, Prassl AJ, Chen J, Kickinger F, Kohl P, Plank G, Trayanova N, Image-based models of cardiac structure in health and disease. *WIREs Syst Biol Med*. 2010 2 489-506.

55) http://www.froedtert.com/HealthResources/ReadingRoom/EveryDay/May-July2006Issue/ICDImplantsforHeartFailure.htm

56) Bajaj C., Goswami S., Yu Z., Zhang Y., Bazilevs Y., Hughes T.J.R. Patient specific heart models from high resolution CT. *CompIMAGE*. Coimbra, Portugal. October 20-21, 2006.

57) Dey T.K., Goswami S. Tight Cocone: A water-tight surface reconstructor. In *Proc. 8th ACM Sympos. Solid Modeling and Applications*, pp-127-134 (2003).

58) Trayanova N., Eason J., Aguel F., Computer simulations of cardiac defibrillation: A look inside the heart. *Comput Visual Sci* 4:259-270 (2002).

59) Hung J. Francois C., Nelson NA, Young A., Cowan BR., Jerecic R., Carr J., Cardiac image modeling tool for quantitative analysis of global and regional cardiac wall motion. *Invest Radiol* 2009;44: 271–278.

60) Prassl AJ, Kickinger F, Ahammer H, Grau V, Schneider JE, Hofer E, Vigmond EJ, Trayanova NA, Plank G. Automatically generated, anatomically accurate meshes for cardiac electrophysiology problems. IEEE Trans Biomed Eng. 2009 May; 56(5): 1318.